Travail de Fin d'Etudes : Investigations on the modeling of bridge deck flutter by means of fractional derivatives

Auteur : Theunissen, Kevin
Promoteur(s) : Denoel, Vincent
Faculté : Faculté des Sciences appliquées
Diplôme : Master en ingénieur civil des constructions, à finalité spécialisée en "civil engineering"
Année académique : 2019-2020
URI/URL : http://hdl.handle.net/2268.2/9016

UNIVERSITY OF LIÈGE

FACULTY OF APPLIED SCIENCES

Investigations on the modeling of bridge deck flutter by means of fractional derivatives

Master Thesis in order to obtain the Master's degree
Civil Engineer in Construction

Kevin Theunissen

Supervisor :

Vincent Denoël - ULiège

Jury members :

Thomas Andrianne - ULiège

Grigorios Dimitriadis - ULiège

Yves Duchêne - Bureau Greisch

Academic year 2019-2020

Acknowledgements

I wish to thank all my professors for sharing their knowledge and experience during all these years and especially my supervisor Mr Vincent Denoël who followed me through this Master thesis and gave me helpful advice to reach the purpose of this work.

I would like to thank Mr Anass Mayou, the PhD student who helped me to deal with the thematic of this Master thesis. His kindness and his availability enormously contributed towards the quality of this work.

I would like to thank all jury members for having accepted to read this Master thesis.

My gratitude also goes to my sister, my parents, my grandparents and my friends for their incredible support. They are a great source of inspiration and motivation.

Kevin Theunissen,
June 2020

Abstract

The flutter velocity is an important output for the design of long-span bridges. Jones proposed in 1940 a model based on rational derivatives for the determination of this velocity.

Through this Master thesis, a model based on fractional derivatives is considered. In the context of the flat plate theory, the accuracy of this model is compared to the one of the Jones' model in order to represent the Theodorsen's function. Then follows a discussion in the frequency domain and in the time domain, stochastic analysis versus simulation based approach, where the results of the flutter speeds are confronted for two degree-of-freedom system. Finally, a case study of a real bridge is presented. The bridge is reduced to its torsional-degree-of-freedom system subjected to a pitch moment. The flutter derivatives obtained experimentally are approximated by the fractional model for the computation of the structural response.

Résumé

La vitesse de flottement est une donnée importante du dimensionnement des ponts à grande portée. En 1940, Jones a proposé un modèle basé sur les dérivées entières afin de déterminer cette vitesse.

Au travers de cette thèse de Master, un modèle aux dérivées fractionnaires est considéré. Dans le contexte de la théorie de la plaque mince, la précision de ce modèle est comparée à celle du modèle proposé par Jones dans le but d'approximer la fonction de Theodorsen. S'ensuit ensuite une discussion dans le domaine fréquentiel et dans le domaine temporel, confrontation entre analyse stochastique et approche par simulation, où les résultats des vitesses de flottement sont comparés entre eux pour un système à deux degrés de liberté. Enfin, un cas d'étude d'un réel pont est présenté. Ce pont est réduit à son système à un degré de liberté en torsion soumis à un moment. Les coefficients de flottement obtenus expérimentalement sont approximés par le modèle aux dérivées fractionnaires afin d'obtenir par calcul la réponse structurelle.

Contents

List of Figures

List of Tables

List of Symbols

θ	Torsion angle of bridge deck
ξ	Damping ratio
ρ	Air density
$\phi(k)$	Jones' function
${}_aD_t^\alpha f(t)$	Riemann-Liouville fractional derivative
B	Deck width
b	Deck half-chord
$C(k)$	Theodorsen's function
c_θ	θ damping
c_z	z damping
$F(k)$	Real part of Theodorsen's function
$G(k)$	Imaginary part of Theodorsen's function
J	Inertia per unit length
K	Reduced circular frequency based on deck width
k	Reduced circular frequency based on deck half-chord
k_θ	θ stiffness
k_z	z stiffness
M	Pitching moment, positive nose up
m	Mass per unit length
$S(k)$	Swinney's model
$S_{aug}(k)$	Augmented Swinney's model
U	Mean velocity of incoming wind
w	Vertical component of incoming turbulence, positive upwards
z	Vertical displacement of bridge deck

1 Introduction

Aerodynamics research is marked by three important turning points [1]. The first one is the simple estimation of the wind pressure based on the wind speed normal to the surface by John Smeaton. The second one was the tragic rupture of the railroad bridge called The Firth of Tay Bridge in Scotland. Due to gust wind loading, it collapsed only two years after its inauguration taking the lives of seventy-five people. The last one is the famous collapse of the Tacoma Bridge in the United States in 1940. This was the starting point of the aerodynamic study. Since then, many researchers have worked on the development of equations to explain this failure. In consequence, new theories have emerged and have become the foundations of the aerodynamic studies in the civil engineering. Many new mathematical models have appeared, including the Jones' model. This model is able to approximate the Theodorsen's function for the flat plate theory, but it is also used to fit the Scanlan's flutter derivatives after wind tunnel tests.

In this Master thesis, the accuracy of two other models is studied compared to the Jones' model. They both use the theory of fractional derivatives. In Chapter 2, The Fractional Derivative Theory is developed and followed by the main concepts of flutter theory in Chapter 3. In that section, the equation of motion is explained as well as the Theodorsen's function. Then Jones' model and its applications are discussed before ending with the Scanlan's flutter derivatives. In Chapter 4, all the previously mentioned theories are combined in order to determine the flutter speed in the frequency and time domains. First, a fitting of the Theodorsen's function is carried out with these two new models before verifying the accuracy compared with the Jones' model. Then, the flutter speed is obtained in the frequency domain. For the time domain analysis, an explicit numerical scheme is used to solve the equation. Finally, the accuracy of both models is assessed. In Chapter 5, the Golden Gate Bridge is chosen in order to illustrate the method for a real bridge. The same method as described above is followed. Based on wind tunnel tests, the Scanlan's flutter derivatives are determined before solving the equation of motion in the frequency and time domains for single degree-of-freedom.

2 Fractional derivatives

This chapter covers the properties needed to solve the equation of motion. Different definitions of a fractional derivative exist, this Master thesis focuses only on the Riemann-Liouville definition but to calculate the results in the time domain, the Grünwald-Letnikov definition is used. Both definitions are identical for a wide class of functions that are commonly encountered in the physical and engineering fields [2].

2.1 Motivation

Fractional derivatives are a tool that extends the concept of linear operator with integer powers. By using a Fourier Transform of the exponential, the answer is always a rational fraction with integer powers. However, a large number of physical laws are not governed by rational derivatives. Indeed, it is possible to express some concepts by using fractional powers [3]. Finally, fractional derivatives can more properly fit natural phenomena. For example, fractional calculus is more and more employed in the modeling of advanced materials [4].

2.2 Properties

Derivatives of Arbitrary Order

$$ {}_aD_t^p f(t) = \frac{1}{\Gamma(k-p)} \frac{d^k}{dt^k} \int_a^t (t-\tau)^{k-p-1} f(\tau) d\tau \tag{1} $$

$(k-1 \leq p < k)$ and k is an integer

First property

$$ {}_aD_t^p ({}_aD_t^{-p} f(t)) = f(t) \tag{2} $$

where $t > a$ and $p > 0$. The equation (2) shows that the Riemann-Liouville fractional differential operator is the left inverse Riemann-Liouville fractional integration operator of the same order p [2].

Second property

It is possible to extend the first property.

$$ {}_aD_t^p({}_aD_t^{-q}f(t)) = {}_aD_t^{p-q}f(t) \tag{3}$$

where $t > a$, $p > q \geq 0$ and that ${}_aD_t^{p-q}f(t)$ exists [2].

Third property

$$ {}_aD_t^{-p}({}_aD_t^q f(t)) = {}_aD_t^{q-p}f(t) - \sum_{j=1}^{k}[{}_aD_t^{q-j}f(t)]_{t=a}\frac{(t-a)^{p-j}}{\Gamma(p-j+1)} \tag{4}$$

where $t > a$ and $0 \leq k-1 \leq q < k$ [2].

Fourth property

It is possible to combine integer derivatives and fractional derivatives:

$$ \frac{d^n}{dt^n}({}_aD_t^p f(t)) = {}_aD_t^{p+n}f(t) \tag{5}$$

where n is an integer [2].

2.3 Numerical approach

The Grünwald-Letnikov Definition

$$ {}_aD_t^\alpha f(t) = \lim_{h\to 0}\frac{{}_a\Delta_h^\alpha f(t)}{h^\alpha} \tag{6}$$

where

$$ {}_a\Delta_h^\alpha f(t) = \sum_{j=0}^{[\frac{t-a}{h}]}(-1)^j \begin{pmatrix} a \\ j \end{pmatrix} f(t-jh) \tag{7}$$

where the notation $[x]$ represents the integer part of x [2].

Fractional Difference Approach

In this Master thesis, the Grünwald-Letnikov definition is used. The following approximation is obtained [2]:

$$ {}_aD_t^\alpha f(t) \approx {}_a\Delta_h^\alpha f(t) \tag{8}$$

where $0 \leq \alpha < 1$ and the order of approximation is equal to $O(h)$.

Higher-order approximations

$$ {}_0D_t^{\alpha} f(t) = h^{-\alpha} \sum_{k=0}^{[t/h]} w_k^{(\alpha)} f(t - kh) \tag{9} $$

where $k = 0, 1, 2, ..., n$; $n = \left[\frac{t}{h}\right]$ and $w_k^{(\alpha)} = (-1)^j \begin{pmatrix} a \\ j \end{pmatrix}$ [2].

Computation of coefficients

The following expression is used to compute the coefficients $w_k^{(\alpha)}$ [2]:

$$ w_0^{(\alpha)} = 1; w_k^{(\alpha)} = \left(1 - \frac{\alpha + 1}{k}\right) w_{k-1}^{(\alpha)} \tag{10} $$

Initial conditions

If $0 \leq n - 1 \leq \alpha < n$ and if ${}_0D_t^{\alpha} f(t) = h^{-\alpha} \sum_{k=0}^{[t/h]} w_k^{(\alpha)} f(t - kh)$, then n homogeneous initial conditions have to be provided. If these initial conditions are inhomogeneous, it is possible to apply the formula (11) to transform them into homogeneous initial conditions [5]. For further examples, see also [6].

$$ y(x) = \sum_{k=0}^{n-1} b_k x^k + z(x) \tag{11} $$

where $y(x)$ is the initial unknown of the problem, b_k are the inhomogeneous initial conditions and $z(x)$ is the new unknown with homogeneous initial conditions.

To study the Grünwald-Letnikov definition in details, two examples of equations using the fractional operator with theoretical values are presented [7].

Example 1

$$ {}_0D_x^{1/2} y(x) = -y(x) \tag{12} $$

where the initial condition is $y(0) = 1$.

By using the finite difference method [2] and thanks to Equation (9) and Equation (11), Equation (12) can be numerically solved :

$$
\begin{aligned}
&{}_0D_x^{1/2} z(x) + z(x) + 1 = 0 \\
&\Leftrightarrow h^{-1/2} \sum_{k=0}^{n} w_k \cdot z_{n-k} + z_n = -1 \\
&\Leftrightarrow w_0 \cdot z_n + \sum_{k=1}^{n} w_k \cdot z_{n-k} + h^{1/2} z_n = -h^{1/2} \\
&\Leftrightarrow z_n (1 + h^{1/2}) = -h^{1/2} - \sum_{k=1}^{n} w_k \cdot z_{n-k} \\
&\Leftrightarrow z_n = \left(-h^{1/2} - \sum_{k=1}^{n} w_k \cdot z_{n-k} \right) / (1 + h^{1/2})
\end{aligned}
$$

where $n = x/h$ and h is the time step. This method is called 'Traditional'. However, Podlubny proposed another method [2] :

$$
\begin{aligned}
&{}_0D_x^{1/2} z(x) + z(x) + 1 = 0 \\
&\Leftrightarrow h^{-1/2} \sum_{k=0}^{n} w_k \cdot z_{n-k} + z_{n-1} = -1 \\
&\Leftrightarrow w_0 \cdot z_n + \sum_{k=1}^{n} w_k \cdot z_{n-k} + h^{1/2} z_{n-1} = -h^{1/2} \\
&\Leftrightarrow z_n = -h^{1/2} - h^{1/2} z_{n-1} - \sum_{k=1}^{n} w_k \cdot z_{n-k}
\end{aligned}
$$

For both methods, $y(x)$ has been transformed into $z(x)$. To calculate the real solution $y(x)$, Equation (13) is used:

$$
y(x) = z(x) + 1 \tag{13}
$$

On Figures 1 and 2, the solution of $y(x)$ for two different steps h is shown.

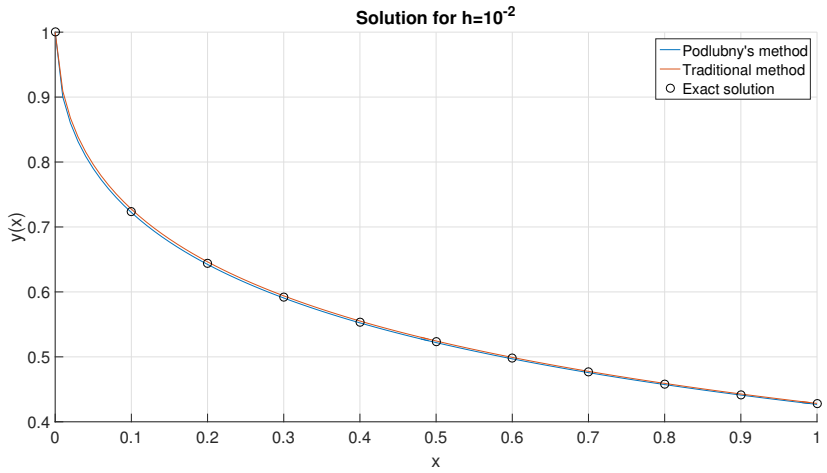

Figure 1: Example 1 : Solution for $h = 10^{-2}$

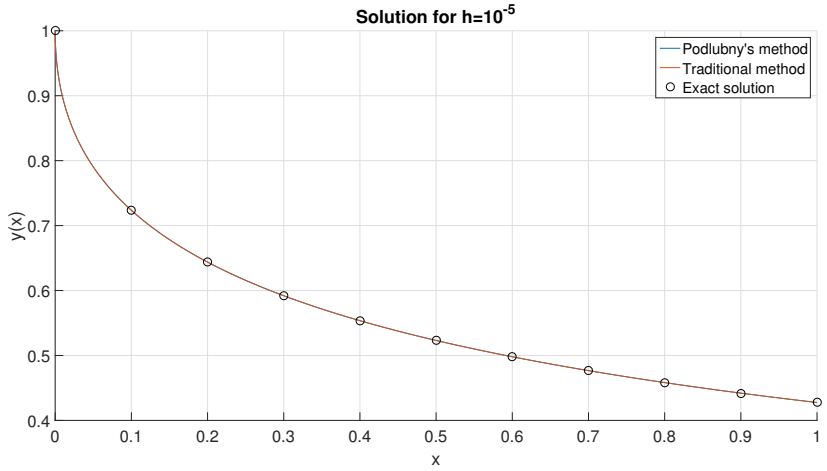

Figure 2: Example 1 : Solution for $h = 10^{-5}$

On Figures 1 and 2, it is clear that for a smaller step h, Podlubny's method is more accurate. To confirm this observation, the absolute error has been calculated and reported on Figures 3 and 4. Equation (14) gives the formula for the calculation of the error :

$$error = \frac{|\text{exact solution} - \text{numerical solution}|}{|\text{exact solution}|} \tag{14}$$

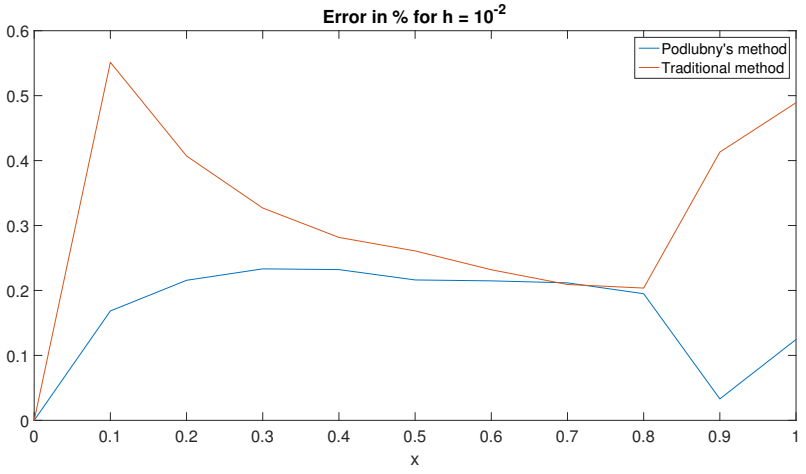

Figure 3: Example 1 : Absolute error for $h = 10^{-2}$

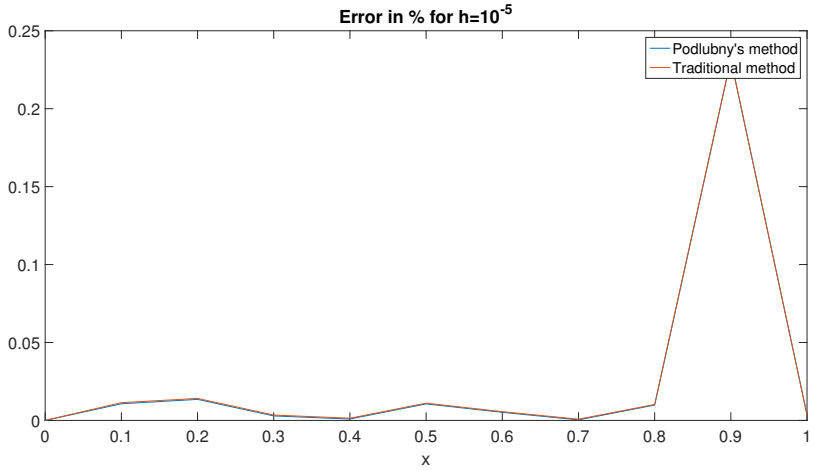

Figure 4: Example 1 : Absolute error for $h = 10^{-5}$

As presented on Figure 5, the absolute errors were calculated for a large amount of steps h. For each step, the Podlubny's method is more accurate than the traditional method and for smaller steps h, the traditional method tends to converge to Podlubny's method.

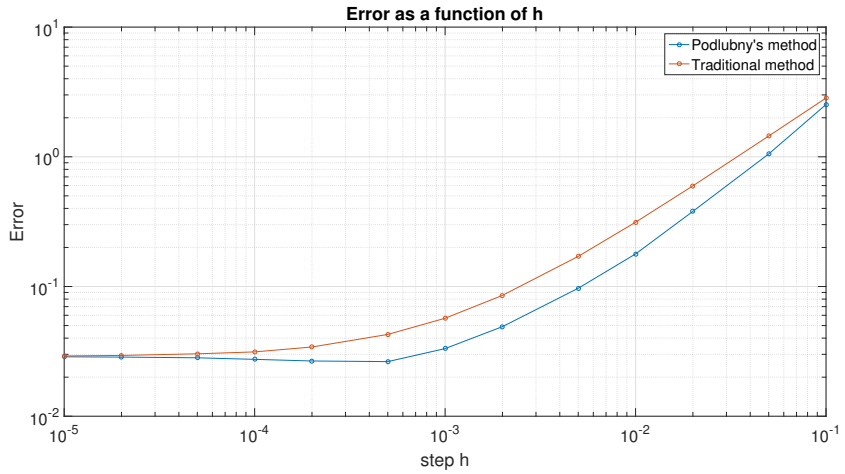

Figure 5: Example 1 : Absolute error for different steps h

Example 2

It is possible to repeat the same exercise but this time, a fractional derivative exponent greater than the unity is taken into account with two initial conditions.

$$ {}_0D_x^{3/2} y(x) = -y(x) \tag{15}$$

where the initial conditions are $y(0) = 1$ and $y'(0) = 0$.

Traditional method :

$$\begin{aligned}
&{}_0D_x^{3/2} z(x) + z(x) + 1 + 0 \cdot x = 0 \\
&\Leftrightarrow h^{-3/2} \sum_{k=0}^{n} w_k \cdot z_{n-k} + z_n = -1 \\
&\Leftrightarrow w_0 \cdot z_n + \sum_{k=1}^{n} w_k \cdot z_{n-k} + h^{3/2} z_n = -h^{3/2} \\
&\Leftrightarrow z_n (1 + h^{3/2}) = -h^{3/2} - \sum_{k=1}^{n} w_k \cdot z_{n-k} \\
&\Leftrightarrow z_n = \left(-h^{3/2} - \sum_{k=1}^{n} w_k \cdot z_{n-k}\right) / (1 + h^{3/2})
\end{aligned}$$

Podlubny's method :

$$\begin{aligned}
&{}_0D_x^{3/2} z(x) + z(x) + 1 + 0 \cdot x = 0 \\
&\Leftrightarrow h^{-3/2} \sum_{k=0}^{n} w_k \cdot z_{n-k} + z_{n-1} = -1 \\
&\Leftrightarrow w_0 \cdot z_n + \sum_{k=1}^{n} w_k \cdot z_{n-k} + h^{3/2} z_{n-1} = -h^{3/2} \\
&\Leftrightarrow z_n = -h^{3/2} - h^{3/2} z_{n-1} - \sum_{k=1}^{n} w_k \cdot z_{n-k}
\end{aligned}$$

By using Equation (13), it is possible to obtain the values of $y(x)$.

On Figures 6 and 7, $y(x)$ is plotted for two different steps h.

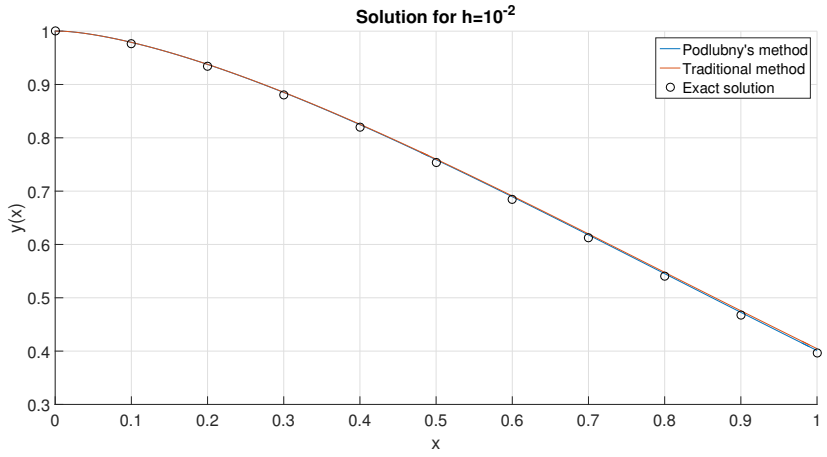

Figure 6: Example 2 : Solution for $h = 10^{-2}$

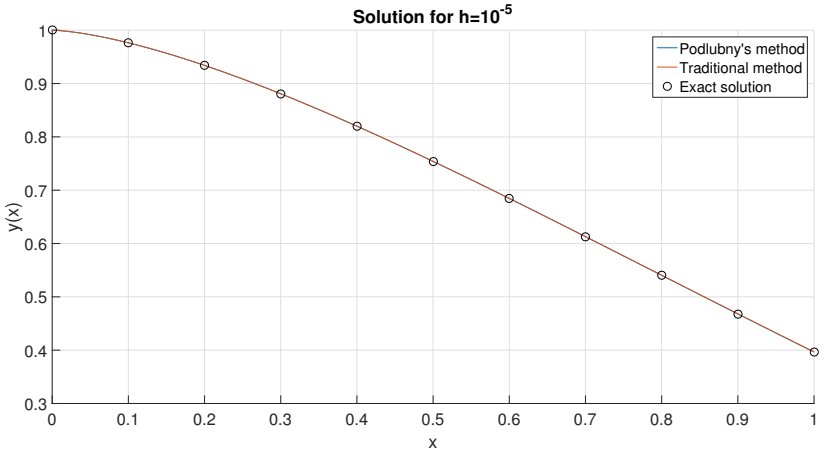

Figure 7: Example 2 : Solution for $h = 10^{-5}$

The same observation can be mentioned : Podlubny's method is more accurate than the traditional one.

On Figures 8 and 9, the absolute errors for $h = 10^{-2}$ and $h = 10^{-5}$ are shown. The formula to calculate the error is the same as Equation (14) previously mentioned.

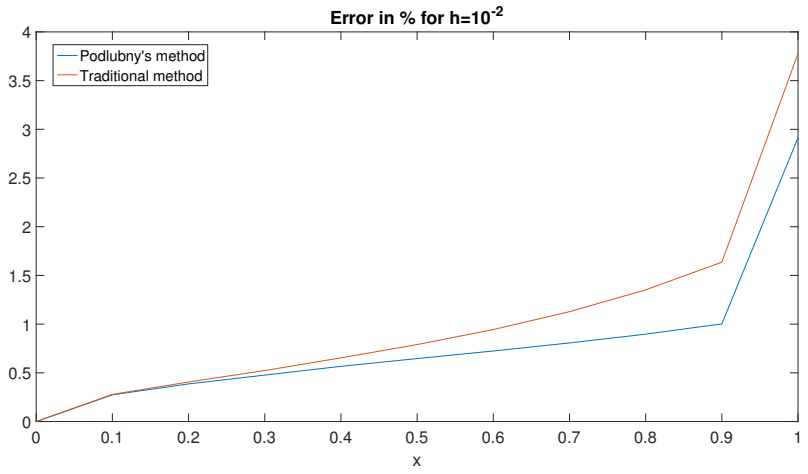

Figure 8: Example 2 : Absolute error for $h = 10^{-2}$

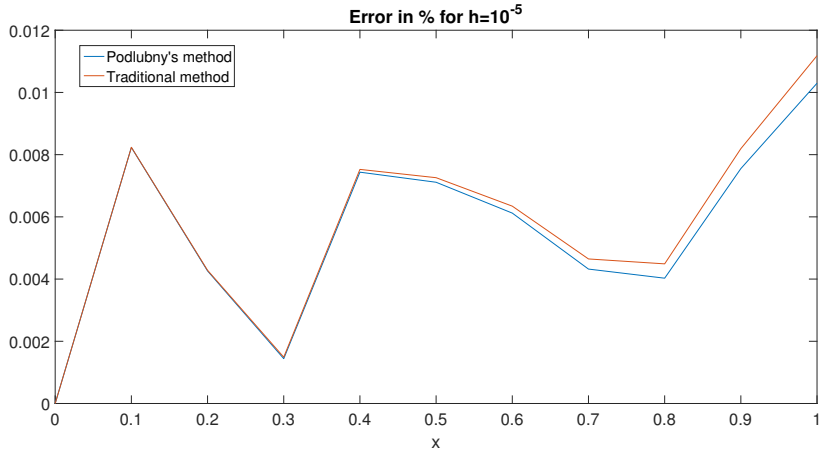

Figure 9: Example 2 : Absolute error for $h = 10^{-5}$

Figure 10 shows the absolute errors that were calculated for different values of step h. Podlubny's method is always more accurate than the traditional method.

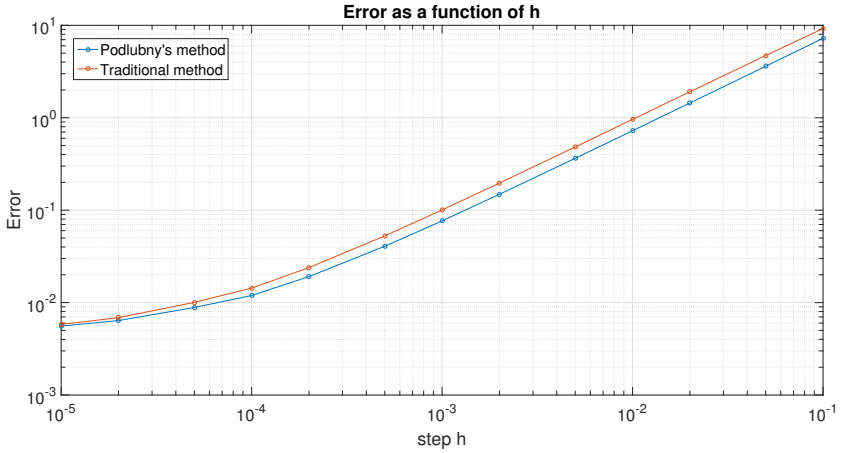

Figure 10: Example 2 : Absolute error for different steps h

Based on the knowledge given by these two examples, it is clear that to improve the solution of a fractional derivatives equation, Podlubny's method has to be used.

3 Flutter of bridge deck

Flutter is a big issue for long-span bridges. This instability comes from wind actions and causes an amplification of the vertical displacements and also of the torsion angle. This effect is directly related to the energy dissipation. If the energy of the aerodynamic forces is greater than the dissipated energy of the mechanical damping, then the displacements increase. If this phenomenon stands during a too long period of time, the structure can collapse [8].

3.1 Equation to solve

The dynamic of the structure is represented on Figure 11:

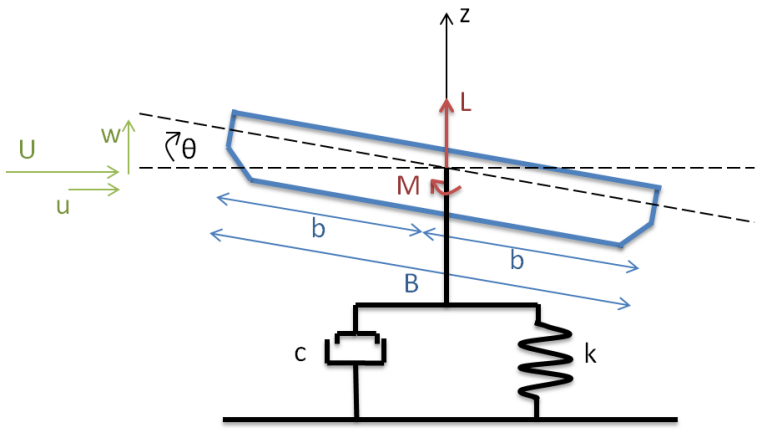

Figure 11: Diagram of the system

On Figure 11, U, u and w are respectively the mean velocity of incoming wind, the horizontal component of incoming turbulence and the vertical component of incoming turbulence while M and L are respectively the pitching moment and the lift force.

The equation (16) is a two degree-of-freedom equation : z the vertical displacement of the bridge deck and θ the torsion angle of the bridge deck [9].

$$\begin{cases} m\ddot{z} + c_z\dot{z} + k_z z = L \\ J\ddot{\theta} + c_\theta\dot{\theta} + k_\theta\theta = M \end{cases} \tag{16}$$

where m is the mass per unit length, J is the inertia per unit length, c_z/c_θ is the damping ratio and k_z/k_θ is the stiffness.

Equation (16) can also be written in the following form [10] :

$$\begin{cases} m\ddot{z} + 4\pi\xi f_z m\dot{z} + 4\pi^2 f_z^2 mz = L \\ J\ddot{\theta} + 4\pi\xi f_\theta J\dot{\theta} + 4\pi^2 f_\theta^2 J\theta = M \end{cases} \tag{17}$$

Wind actions

There is a need to derive the pitching moment and the lift force in details.

$$\begin{cases} L = L_{se} + L_b \\ M = M_{se} + M_b \end{cases} \tag{18}$$

As shown in the equation (18), the pitching moment and the lift force are composed of self-excited forces and buffeting forces.

In this Master thesis, both self-excited forces and buffeting forces are taken into account in order to represent the real behaviour of the bridge. Figure 12 shows the difference between bifurcation, i.e. without buffeting forces, and divergence, i.e. with buffeting forces.

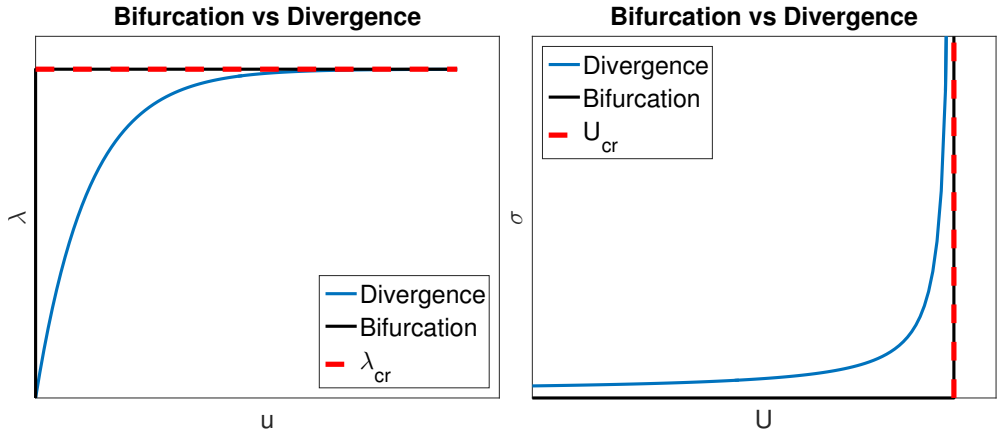

Figure 12: Bifurcation versus Divergence

Buffeting forces

For most bridges cross sections, the horizontal component of incoming turbulence u can be neglected because drag forces are not taken into account in this Master thesis. Buffeting forces L_b and M_b come mainly from the wind turbulence w [1, 11]. The formula in the time domain are given in Equation (19).

$$\begin{cases} L_b(t) = \pi\rho U B\, w(t) \\ M_b(t) = \frac{1}{4}\pi\rho U B^2\, w(t) \end{cases} \tag{19}$$

It is possible to derive the expressions of buffeting forces in frequency domain by using the Fourier Transform of $w(t)$.

$$\begin{cases} L_b(\omega) = \pi\rho U B\, w(\omega) \\ M_b(\omega) = \frac{1}{4}\pi\rho U B^2\, w(\omega) \end{cases} \tag{20}$$

Then, to know $w(\omega)$, the Von Karman Power Spectral Density (PSD) is used by making the following hypotheses (see Equation (21)):

- $w(t)$ is a random process that has a mean value equal to zero
- This random process is Gaussian and stationary

$$S_w(\omega) = \frac{\sigma_w^2 L_w}{\pi U} \frac{1 + 755.2\left(\frac{\omega L_w}{2\pi U}\right)^2}{\left(1 + 283.2\left(\frac{\omega L_w}{2\pi U}\right)^2\right)^{\frac{11}{6}}} \tag{21}$$

Self-excited forces

The self-excited forces come from the motion itself of the bridge deck. The formula in the frequency domain is given by the Equation (22):

$$\left\{ \begin{array}{c} L_{se}(\omega) \\ M_{se}(\omega) \end{array} \right\} = q \left[\begin{array}{cc} \frac{B\omega^2}{4U^2} - C(\omega)\frac{i\omega}{U} & \frac{B}{4U}(i\omega) + C(\omega)\left(1 + \frac{B}{4U}(i\omega)\right) \\ -\frac{B}{4}C(\omega)\frac{i\omega}{U} & \frac{B}{4}\left(\frac{B^2\omega^2}{32U^2} - \frac{B}{4U}(i\omega) + C(\omega)\left(1 + \frac{B}{4U}(i\omega)\right)\right) \end{array} \right] \left\{ \begin{array}{c} z(\omega) \\ \theta(\omega) \end{array} \right\} \tag{22}$$

where $q = \pi\rho U^2 B$ and $C(\omega)$ is the Theodorsen's function.

3.2 Theodorsen's function

Theodorsen's function depends only on $k = \frac{\omega b}{U}$, the reduced circular frequency based on deck half chord. This function is an exact solution of the circulatory aerodynamic forces that are obtained from the harmonic oscillation of a flat plate [12]. There are different formula to evaluate Theodorsen's function. In this Master thesis, the following mathematical equation is used:

$$C(k) = \frac{K_1(ik)}{K_0(ik) + K_1(ik)} \tag{23}$$

where K_n is a modified Bessel function of the third kind of order n.

On Figure 13, the real and imaginary parts of Equation (23) are shown.

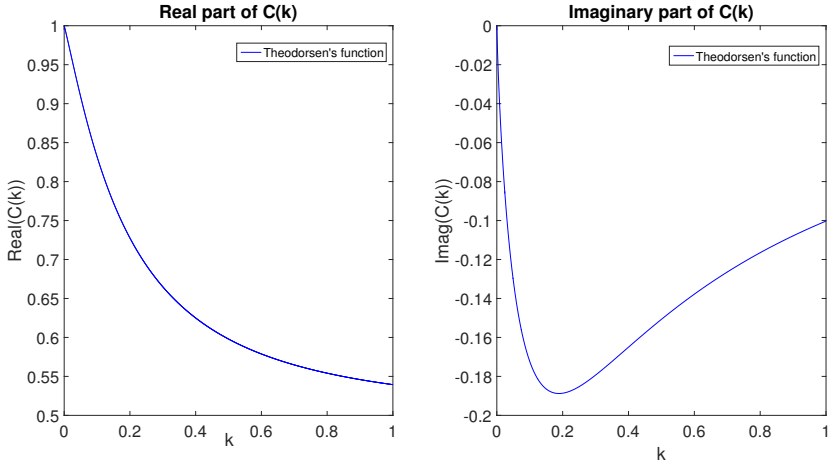

Figure 13: Theodorsen's function

3.3 Jones' model

To approximate the Theodorsen's function, the Jones' model has been developed in 1940 [13]. This model consists, in the time domain, of a sum of decreasing exponentials [14].

$$\phi(s) = 1 - 0.165e^{-0.0455\,s} - 0.335e^{-0.3\,s} \tag{24}$$

where $s = \frac{Ut}{b}$ is a dimensionless time parameter.

In the frequency domain, a Fourier Transform can be used on Equation (24) in order to obtain the Equation (25):

$$\phi(k) = 1 - 0.165\frac{ik}{ik + 0.0455} - 0.335\frac{ik}{ik + 0.3} \tag{25}$$

Figure 14 shows the Jones' approximation compared to the Theodorsen's function. In Chapter 4, a complete discussion about this model will be done.

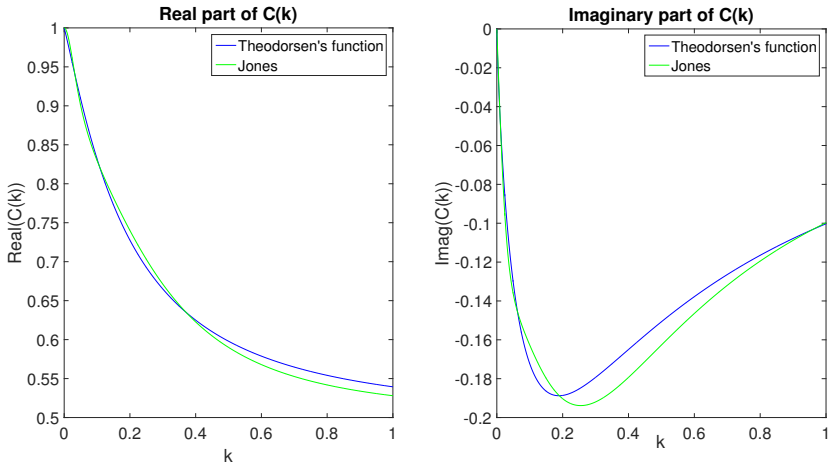

Figure 14: Jones' approximation and Theodorsen's function

3.4 Scanlan's flutter derivatives

In 1971, Scanlan and Tomko derived a new formulation of the self-excited forces for a two-dimensional bridge deck section [9].

$$\begin{cases} L_{se}(t) = qB\left[KH_1^*(K)\frac{\dot{z}(t)}{U} + KH_2^*(K)\frac{B\dot{\theta}(t)}{U} + K^2H_3^*(K)\theta(t) + K^2H_4^*(K)\frac{z(t)}{U}\right] \\ M_{se}(t) = qB^2\left[KA_1^*(K)\frac{\dot{z}(t)}{U} + KA_2^*(K)\frac{B\dot{\theta}(t)}{U} + K^2A_3^*(K)\theta(t) + K^2A_4^*(K)\frac{z(t)}{U}\right] \end{cases} \tag{26}$$

where $q = 0.5\rho U^2$ is the dynamic pressure.

Here is the formulation for all Scanlan's flutter derivatives :

$$\begin{aligned} H_1^*(K) &= \pi\left[\frac{2F(k)}{K}\right] \\ H_2^*(K) &= \pi\left[\frac{2G(k)}{K^2} + \frac{1}{2K} + \frac{F(k)}{2K}\right] \\ H_3^*(K) &= \pi\left[\frac{2F(k)}{K^2} - \frac{G(k)}{2K}\right] \\ H_4^*(K) &= \pi\left[-\frac{1}{2} - \frac{2G(k)}{K}\right] \end{aligned} \qquad \begin{aligned} A_1^*(K) &= \pi\left[\frac{F(k)}{2K}\right] \\ A_2^*(K) &= \pi\left[-\frac{1}{8K} + \frac{G(k)}{2K^2} + \frac{F(k)}{8K}\right] \\ A_3^*(K) &= \pi\left[\frac{1}{64} + \frac{F(k)}{2K^2} - \frac{G(k)}{8K}\right] \\ A_4^*(K) &= \pi\left[-\frac{G(k)}{2K}\right] \end{aligned}$$

However, the Equation (26) is a mixed of time domain and frequency domain. Starossek developed a compact formulation in the frequency domain for the self-excited forces [15].

$$\begin{cases} L = \omega^2 \pi \rho b^2 (c_{zz} z + b c_{z\theta} \theta) \\ M = \omega^2 \pi \rho b^2 (b c_{\theta z} z + b^2 c_{\theta\theta} \theta) \end{cases} \tag{27}$$

where,

- $c_{zz} = 1 - \frac{2i}{k} C(k) = \frac{2}{\pi}(H_4^* + iH_1^*)$
- $c_{z\theta} = -\frac{1}{k}[i(C(k)+1) + \frac{2}{k} C(k)] = \frac{4}{\pi}(H_3^* + iH_2^*)$
- $c_{\theta z} = \frac{i}{k} C(k) = \frac{4}{\pi}(A_4^* + iA_1^*)$
- $c_{\theta\theta} = \frac{i}{2k}(C(k) - 1) + \frac{1}{k^2} C(k) + \frac{1}{8} = \frac{8}{\pi}(A_3^* + iA_2^*)$

4 Application of fractional derivatives to the flat plate theory

In this chapter, the fitting of Theodorsen's function is discussed as well as its impact on the computation of the flutter speed. The Storebaelt Bridge in Denmark is taken as an example to analyse the results in the context of the flat plate theory. Firstly, a comparison between fractional derivatives models and Jones' model is carried out. Then, flutter analysis is made in frequency domain. It is therefore possible to evaluate the accuracy of all models. The last step in this chapter concerns the solution in the time domain. The numerical approach is analysed through the equation of motion to calculate the flutter speed.

4.1 Fitting of the Theodorsen's function

The fitting of the Theodorsen's function is a good starting point to correctly evaluate the flutter speed. In 1989, David V. Swinney proposed a fractional model based on only two parameters [12]:

$$S(k) = \frac{1 + a(i\omega)^{\alpha}}{1 + 2a(i\omega)^{\alpha}} \tag{28}$$

where $a = 2.19$ and $\alpha = \frac{5}{6}$.

This model provides a good approximation of the Theodorsen's function. In this Master thesis, a new fractional model is proposed based on Swinney's model. This model is called *augmented Swinney* because four parameters are used instead of two.

$$S_{aug}(k) = \frac{1 + a(i\omega)^{\alpha} + b(i\omega)^{\beta}}{1 + 2a(i\omega)^{\alpha} + 2b(i\omega)^{\beta}} \tag{29}$$

where $a = 1.9293$, $b = 0.4262$, $\alpha = 0.7887$ and $\beta = 1.4753$.

The main goal of this model is to improve Swinney's fitting of the Theodorsen's function. Moreover, this model contains the same number of parameters than the Jones' model approximation of the Theodorsen's function. If for the same number of parameters the augmented Swinney's approximation is better then, the application of this new model could be extended to the fitting of the Scanlan's flutter derivatives for example.

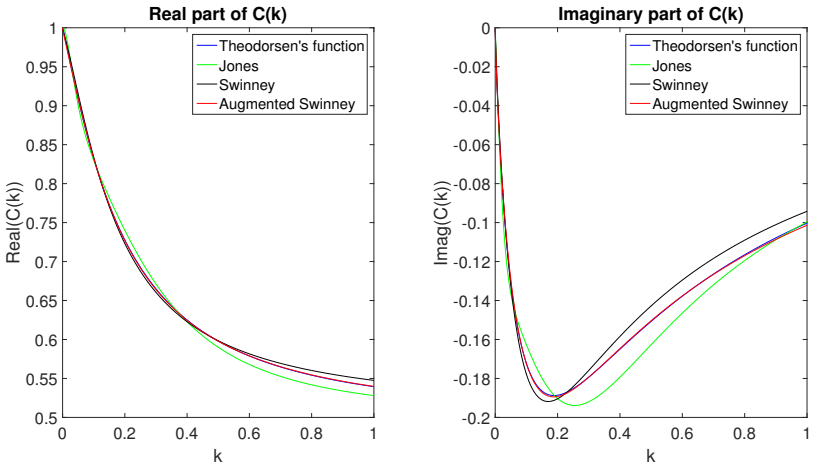

Figure 15: Comparison of the three different models' approximations based on the Theodorsen's function

On Figure 15, Jones', Swinney's and augmented Swinney's approximations are shown and can be compared to the reference function given by Equation (23).

Equation (30) represents the error of the three different models.

$$\text{error} = \sqrt{\sum \left|\text{reference function - model}\right|^2} \tag{30}$$

Table 1 contains the models' approximation errors.

Model	Error
Jones' model	$1.29e^{-2}$
Swinney's model	$7.90e^{-3}$
Augmented Swinney's model	$8.32e^{-4}$

Table 1: Error of the different models' approximations on the fitting of Theodorsen's function

It is now possible to come to a first conclusion about the fitting of Theodorsen's function. All fractional models' approximation are more accurate than Jones' model's. Moreover, augmented Swinney's approximation is able to fit almost perfectly with the Theodorsen's function by using the same amount of parameters as Jones' model. A comparison of these models is going to be made in the frequency domain and it will be seen if this observation is confirmed by calculating the flutter speed.

4.2 Frequency domain

In this chapter, the Storebaelt Bridge in Denmark is taken as an example. The main span is equal to 1624 meters and the structure connects Seeland and Fionie islands. The following used values are reported in Table 2 (see [16]):

	Value	Unit
m	22740	kg/m
J	$2.41 \cdot 10^6$	$kg \cdot m^2/m$
B	31	m
ξ	0.003	$-$
f_z	0.10	Hz
f_θ	0.278	Hz
ρ	1.22	kg/m^3
L_w	20	m
U	$[10, 80]$	m/s
I_w	0.05	$-$

Table 2: Storebaelt Bridge values

The equation that has to be solved is given by Equation (17), Equation (20) for the buffeting forces and Equation (22) for the self-excited forces.

On Figure 16, the PSD for each model are shown. PSD gives a good idea of how accurate a model is and if the real behaviour of the structure is correctly represented. The PSD is a representation of the structural response for a given frequency.

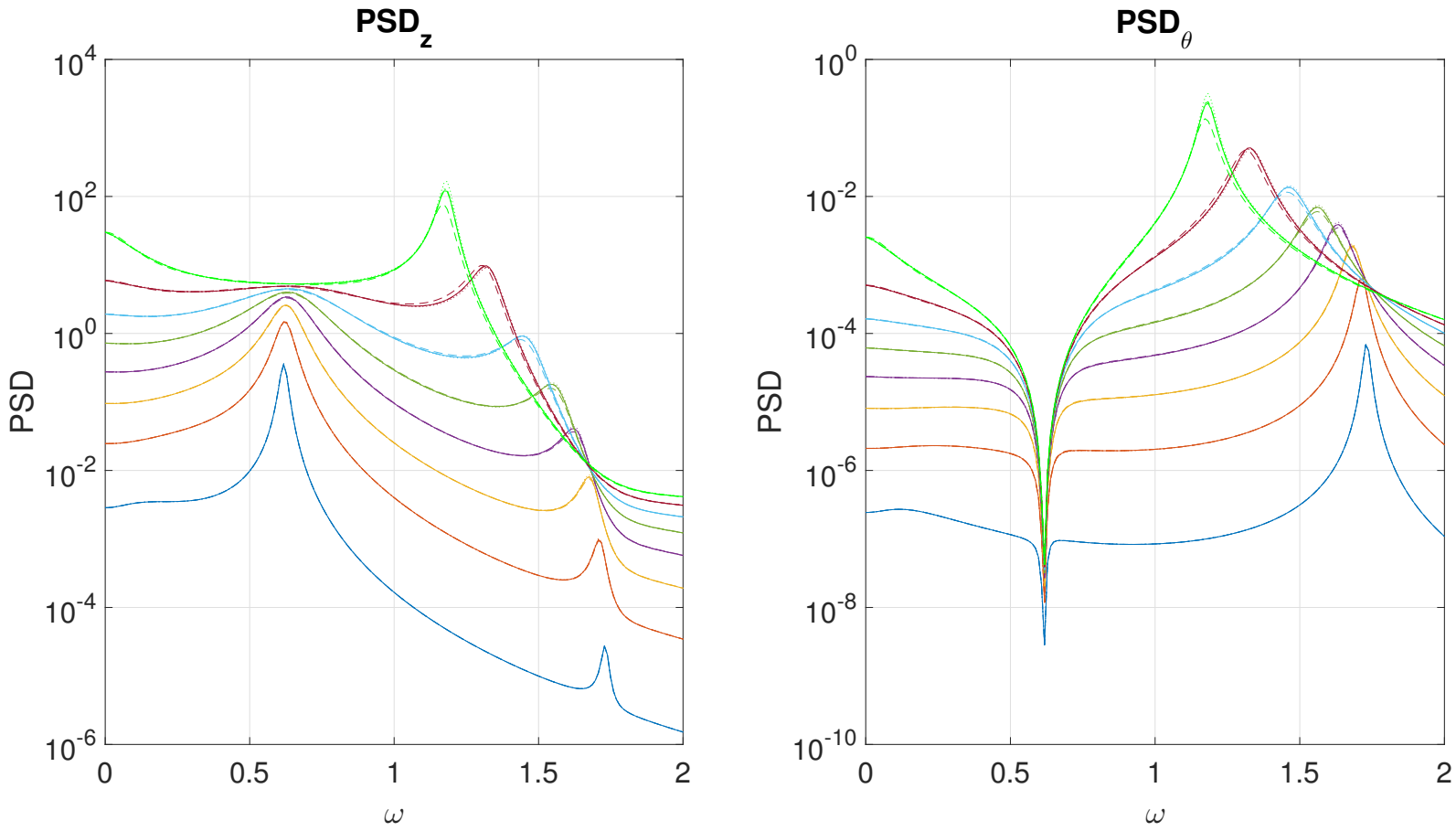

Figure 16: PSD of the different models in frequency domain

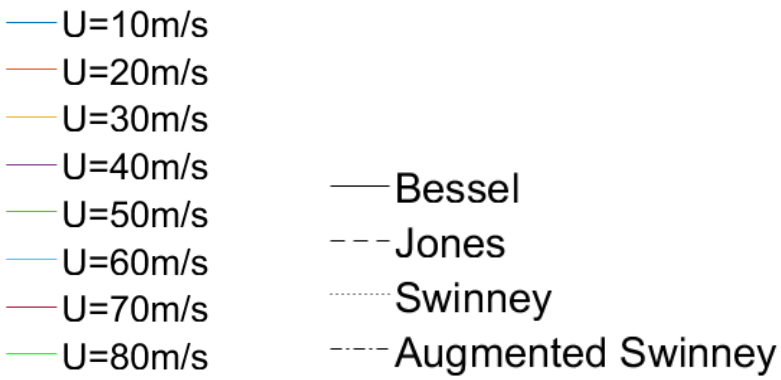

Figure 17: Legend of PSD in frequency domain

On Figure 16, several observations can be noticed:

- For lower wind speeds, all PSD given by the models fit properly the reference PSD.
- For greater wind speeds, Jones' approximation is the less accurate especially around peaks.
- PSD for both fractional derivatives models are close to the reference PSD and as expected, augmented Swinney's model is the most accurate.

To determine the flutter speed, the standard deviation needs to be calculated. Equation (31) gives its formula [17].

$$\sigma_x = \sqrt{\int_{-\infty}^{+\infty} PSD_x(\omega) d\omega} \tag{31}$$

The flutter speed occurs when the standard deviation is at its maximum.

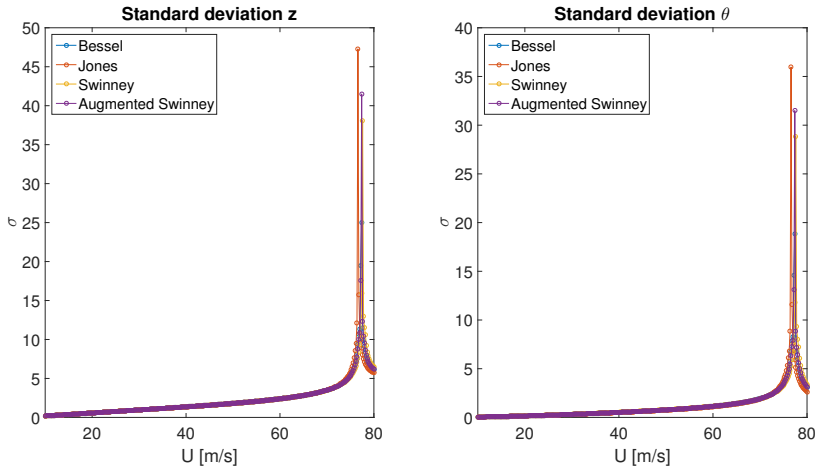

Figure 18: Standard deviation given by the different models in frequency domain

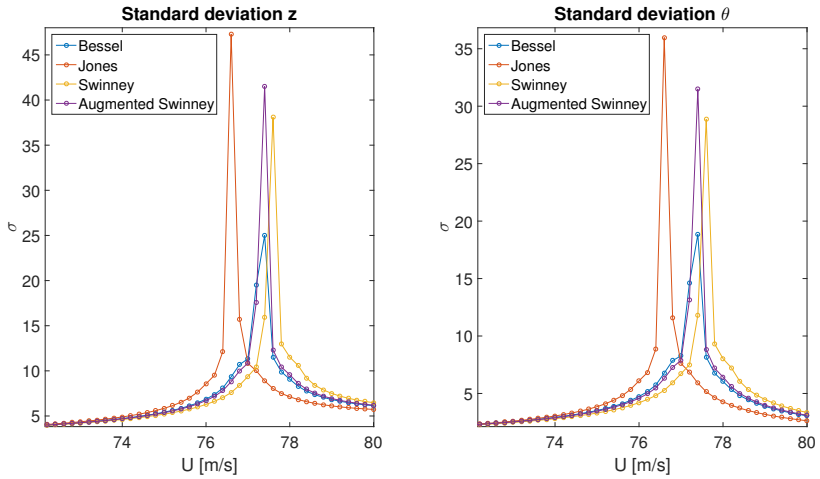

Figure 19: Zoom standard deviation given by the different models in frequency domain

Table 3 contains the different flutter speeds of each model.

Model	Flutter speed [m/s]
Theodorsen's function	77.4
Jones	76.6
Swinney	77.6
Augmented Swinney	77.4

Table 3: Flutter speed for all different models

Based on Figures 18 and 19 and Table 3, it is now clear that Jones' approximation is the least accurate approximation based on the reference function (Theodorsen's function). However, the difference is quite small. Indeed, it is lower than 1 m/s.

On Figure 20, the error is plotted based on the Theodorsen's function. Instead of calculating the error as a function of the wind speed U, it is more interesting to determine the error as a function of the standard deviation. Actually, the flutter speed is given for the standard deviation maximum. It is more relevant if, for a given standard deviation, the model can give an accurate wind speed U.

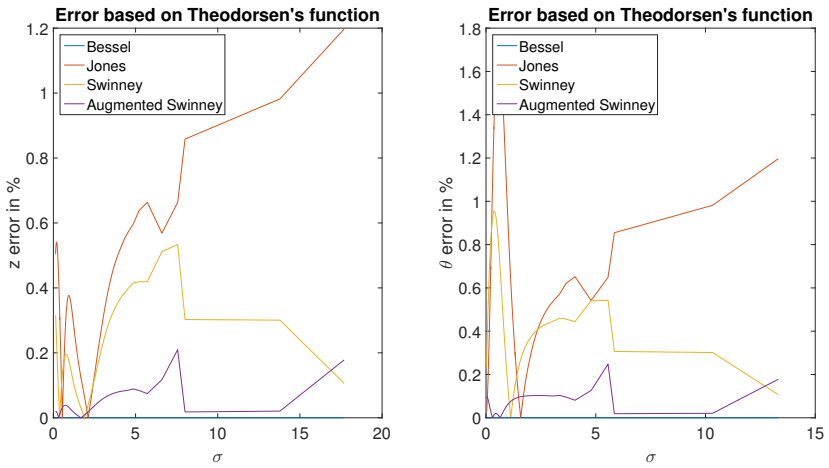

Figure 20: Error on the flutter speed of the different models in frequency domain

The errors of all models are really low : maximum 1.5% for Jones' model. As expected again, augmented Swinney's model is the most accurate model but compared to other models, the increasing in precision is not very relevant.

4.3 Time domain

In this section, the Monte Carlo method for fractional derivatives models is discussed. The flutter speed is determined for all models and compared to the reference solution. Afterwards, the discussion is focused on numerical calculation time and optimization and truncation.

Flutter speed analysis

Before showing the results, it is interesting to focus on the main mathematic points. Jones' is the first model that is discussed.

By using Equation (22), it is possible to derive the self-excited forces in time domain :

$$\begin{aligned} L_{se}(\omega) &= \pi\rho U^2 B\left[\left(\tfrac{B}{4U}(i\omega)\theta(\omega)+\tfrac{B\omega^2}{4U^2}z(\omega)\right)+C(\omega)\left(\theta(\omega)-(i\omega)\tfrac{z(\omega)}{U}+(i\omega)\tfrac{B}{4U}\theta(\omega)\right)\right] \\ &= \pi\rho U^2 B\left[\left(\tfrac{B}{4U}(i\omega)\theta(\omega)+\tfrac{B\omega^2}{4U^2}z(\omega)\right)+\tfrac{C(\omega)}{(i\omega)}\left((i\omega)\theta(\omega)+\omega^2\tfrac{z(\omega)}{U}-\omega^2\tfrac{B}{4U}\theta(\omega)\right)\right] \end{aligned}$$

By applying the Fourier transform,

$$L_{se}(t) = \pi\rho U^2 B\left[\left(\tfrac{B}{4U}\dot{\theta}(t)-\tfrac{B}{4U^2}\ddot{z}(t)\right)+\int_0^t\phi(t-\tau)\left(\dot{\theta}(\tau)-\tfrac{\ddot{z}(\tau)}{U}+\tfrac{B\ddot{\theta}(\tau)}{4U}\right)d\tau\right]$$

Suggesting that

$$exp(t)=\int_0^t\phi(t-\tau)\left(\dot{\theta}(\tau)-\frac{\ddot{z}(\tau)}{U}+\frac{B\ddot{\theta}(\tau)}{4U}\right)d\tau \tag{32}$$

and,

$$\mu(t)=\int_0^t\phi(t-\tau)\dot{\theta}(\tau)d\tau \tag{33}$$

$$\nu(t)=\int_0^t\phi(t-\tau)\left(-\frac{\ddot{z}(\tau)}{U}+\frac{B\ddot{\theta}(\tau)}{4U}\right)d\tau \tag{34}$$

where

$$\mu(t)=\sum_{i=0}^{2}\mu_i(t) \tag{35}$$

$$\nu(t)=\sum_{i=0}^{2}\nu_i(t) \tag{36}$$

Moreover, it is possible to express $\dot{\mu}(t)$ and $\dot{\nu}(t)$ as a function of $\mu(t)$ and $\nu(t)$:

$$\dot{\mu}_i(t) = a_i\dot{\theta}(t) - \frac{2b_iU}{B}\mu_i(t) \tag{37}$$

$$\dot{\nu}_i(t) = a_i\left(-\frac{\ddot{z}(\tau)}{U} + \frac{B\ddot{\theta}(\tau)}{4U}\right) - \frac{2b_iU}{B}\nu_i(t) \tag{38}$$

where a_i and b_i are Jones' coefficients.

Then, the following self-excited forces can be obtained :

$$L_{se}(t) = \pi\rho U^2 B\left(\frac{B}{4U}\dot{\theta}(t) - \frac{B}{4U^2}\ddot{z}(t)\right) + \pi\rho U^2 B(\mu_0 + \mu_1 + \mu_2 + \nu_0 + \nu_1 + \nu_2) \tag{39}$$

$$\begin{aligned} M_{se}(t) = {} & \frac{\pi\rho U^2 B^2}{4}\left(\frac{B}{4U^2}\ddot{z}(t) - \frac{B}{2U}\dot{\theta}(t) - \frac{B^2}{32U^2}\ddot{\theta}(t)\right) + \frac{\pi\rho U^2 B^2}{4}\left(\frac{B}{4U}\dot{\theta}(t) - \frac{B}{4U^2}\ddot{z}(t)\right) \\ & + \frac{\pi\rho U^2 B^2}{4}(\mu_0 + \mu_1 + \mu_2 + \nu_0 + \nu_1 + \nu_2) \end{aligned} \tag{40}$$

Finally, the following system of equations has to be solved :

$$\begin{cases} m\ddot{z}(t) + c_z\dot{z}(t) + k_z z(t) = L_{se}(t) + L_b(t) \\ J\ddot{\theta}(t) + c_\theta\dot{\theta}(t) + k_\theta\theta(t) = M_{se}(t) + M_b(t) \end{cases} \tag{41}$$

At last, the following matrix system is derived :

$$\boldsymbol{M}\dot{\boldsymbol{x}}(t) = \boldsymbol{A}\boldsymbol{x}(t) + \boldsymbol{f}_b(t) \tag{42}$$

The expressions of the matrices and vectors can be found in Appendix A1.

Now, the focus is going to be on the fractional derivatives models. Augmented Swinney's model is developed below.

$$\begin{cases} -m\omega^2 z(\omega) + c_z(i\omega)z(\omega) + k_z z(\omega) = L_{se}(\omega) + L_b(\omega) \\ -J\omega^2\theta(\omega) + c_\theta(i\omega)\theta(\omega) + k_\theta\theta(\omega) = M_{se}(\omega) + M_b(\omega) \end{cases} \tag{43}$$

where $L_{se}(\omega)$ and $M_{se}(\omega)$ are given by Equation (22) and where,

$$C(k) = S_{aug}(k) = \frac{1 + a\cdot(i\omega)^\alpha + b\cdot(i\omega)^\beta}{1 + 2a\cdot(i\omega)^\alpha + 2b\cdot(i\omega)^\beta}$$

By multiplying Equation (43) by the augmented Swinney's denominator and by applying the Inverse Fourier Transform, Equation (44) is obtained :

$$\begin{aligned}
&mD_t^2 z(t) + 4\pi f_z \xi m D_t^1 z(t) + 4\pi^2 f_z^2 m z(t) \\
&+2ar^\alpha m D_t^{2+\alpha} z(t) + 8ar^\alpha \pi f_z \xi m D_t^{1+\alpha} z(t) + 8ar^\alpha \pi^2 f_z^2 m D_t^\alpha z(t) \\
&+2br^\beta m D_t^{2+\beta} z(t) + 8br^\beta \pi f_z \xi m D_t^{1+\beta} z(t) + 8br^\beta \pi^2 f_z^2 m D_t^\beta z(t) \\
&= -pr^2 D_t^2 z(t) - 2apr^{2+\alpha} D_t^{2+\alpha} z(t) - 2bpr^{2+\beta} D_t^{2+\beta} z(t) \\
&-2pr D_t^1 z(t) - 2apr^{1+\alpha} D_t^{1+\alpha} z(t) - 2bpr^{1+\beta} D_t^{1+\beta} z(t) \\
&+pBr D_t^1 \theta(t) + \frac{3}{2} apBr^{1+\alpha} D_t^{1+\alpha} \theta(t) + \frac{3}{2} bpBr^{1+\beta} D_t^{1+\beta} \theta(t) \\
&+pB\theta(t) + apBr^\alpha D_t^\alpha \theta(t) + bpBr^\beta D_t^\beta \theta(t) \\
&+f_b(t) + 2ar^\alpha D_t^\alpha f_b(t) + 2br^\beta D_t^\beta f_b(t)
\end{aligned} \tag{44}$$

A similar development can be carried out for the second equation. The new expression is given by Equation (45) :

$$\begin{aligned}
&JD_t^2 \theta(t) + 4\pi f_\theta \xi J D_t^1 \theta(t) + 4\pi^2 f_\theta^2 J\theta(t) \\
&+2ar^\alpha J D_t^{2+\alpha} \theta(t) + 8ar^\alpha \pi f_\theta \xi J D_t^{1+\alpha} \theta(t) + 8ar^\alpha \pi^2 f_\theta^2 J D_t^\alpha \theta(t) \\
&+2br^\beta J D_t^{2+\beta} \theta(t) + 8br^\beta \pi f_\theta \xi J D_t^{1+\beta} \theta(t) + 8br^\beta \pi^2 f_\theta^2 J D_t^\beta \theta(t) \\
&= -\frac{pB}{2} r D_t^1 z(t) - \frac{apB}{2} r^{\alpha+1} D_t^{\alpha+1} z(t) - \frac{bpB}{2} r^{\beta+1} D_t^{\beta+1} z(t) \\
&-\frac{pB^2}{32} r^2 D_t^2 \theta(t) - \frac{apB^2}{16} r^{\alpha+2} D_t^{\alpha+2} \theta(t) - \frac{bpB^2}{16} r^{\beta+2} D_t^{\beta+2} \theta(t) \\
&-\frac{apB^2}{8} r^{\alpha+1} D_t^{\alpha+1} \theta(t) - \frac{bpB^2}{8} r^{\beta+1} D_t^{\beta+1} \theta(t) \\
&+\frac{pB^2}{4} \theta(t) + \frac{apB^2}{4} r^\alpha D_t^\alpha \theta(t) + \frac{bpB^2}{4} r^\beta D_t^\beta \theta(t) \\
&+M_b(t) + 2ar^\alpha D_t^\alpha M_b(t) + 2br^\beta D_t^\beta M_b(t)
\end{aligned} \tag{45}$$

where $r = \frac{B}{2U}$ and $p = \pi\rho U^2$.

By using the finite difference method and by grouping all terms together, the final expression of the solution is derived :

$$
\begin{aligned}
z_n\left(\frac{F_{z2}}{h^2}+\frac{F_{z1}}{h}+\frac{F_{z\alpha 2}}{h^{\alpha+2}}+\frac{F_{z\alpha 1}}{h^{\alpha+1}}+\frac{F_{z\alpha}}{h^{\alpha}}+\frac{F_{z\beta 2}}{h^{\beta+2}}+\frac{F_{z\beta 1}}{h^{\beta+1}}+\frac{F_{z\beta}}{h^{\beta}}\right) \quad (46)\\
-\theta_n\left(\frac{F_{\theta 1}}{h}+\frac{F_{\theta\alpha 1}}{h^{\alpha+1}}+\frac{F_{\theta\beta 1}}{h^{\beta+1}}+\frac{F_{\theta\alpha}}{h^{\alpha}}+\frac{F_{\theta\beta}}{h^{\beta}}\right)\\
=z_{n-1}\left(2\frac{F_{z2}}{h^2}+\frac{F_{z1}}{h}-F_z\right)-\frac{F_{z2}}{h^2}z_{n-2}-\theta_{n-1}\left(\frac{F_{\theta 1}}{h}+F_\theta\right)\\
-\frac{F_{z\alpha 2}}{h^{\alpha+2}}\sum_{j=1}^{n}w_j^{(\alpha+2)}z_{n-j}-\frac{F_{z\alpha 1}}{h^{\alpha+1}}\sum_{j=1}^{n}w_j^{(\alpha+1)}z_{n-j}-\frac{F_{z\alpha}}{h^{\alpha}}\sum_{j=1}^{n}w_j^{(\alpha)}z_{n-j}\\
-\frac{F_{z\beta 2}}{h^{\beta+2}}\sum_{j=1}^{n}w_j^{(\beta+2)}z_{n-j}-\frac{F_{z\beta 1}}{h^{\beta+1}}\sum_{j=1}^{n}w_j^{(\beta+1)}z_{n-j}-\frac{F_{z\beta}}{h^{\beta}}\sum_{j=1}^{n}w_j^{(\beta)}z_{n-j}\\
+\frac{F_{\theta\alpha 1}}{h^{\alpha+1}}\sum_{j=1}^{n}w_j^{(\alpha+1)}\theta_{n-j}+\frac{F_{\theta\beta 1}}{h^{\beta+1}}\sum_{j=1}^{n}w_j^{(\beta+1)}\theta_{n-j}\\
+\frac{F_{\theta\alpha}}{h^{\alpha}}\sum_{j=1}^{n}w_j^{(\alpha)}\theta_{n-j}+\frac{F_{\theta\beta}}{h^{\beta}}\sum_{j=1}^{n}w_j^{(\beta)}\theta_{n-j}\\
+L_{bn}\left(1+2a\frac{r^{\alpha}}{h^{\alpha}}+2b\frac{r^{\beta}}{h^{\beta}}\right)+2a\frac{r^{\alpha}}{h^{\alpha}}\sum_{j=1}^{n}w_j^{(\alpha)}L_{bn-j}+2b\frac{r^{\beta}}{h^{\beta}}\sum_{j=1}^{n}w_j^{(\beta)}L_{bn-j}
\end{aligned}
$$

and for the second equation :

$$
\begin{aligned}
& z_n \left(\frac{G_{z1}}{h} + \frac{G_{z\alpha 1}}{h^{\alpha+1}} + \frac{G_{z\beta 1}}{h^{\beta+1}} \right) \\
& + \theta_n \left(\frac{G_{\theta 2}}{h^2} + \frac{G_{\theta 1}}{h} + \frac{G_{\theta\alpha 2}}{h^{\alpha+2}} + \frac{G_{\theta\alpha 1}}{h^{\alpha+1}} + \frac{G_{\theta\alpha}}{h^{\alpha}} + \frac{G_{\theta\beta 2}}{h^{\beta+2}} + \frac{G_{\theta\beta 1}}{h^{\beta+1}} + \frac{G_{\theta\beta}}{h^{\beta}} \right) \\
& = \frac{G_{z1}}{h} z_{n-1} + \theta_{n-1} \left(2\frac{G_{\theta 2}}{h^2} + \frac{G_{\theta 1}}{h} - G_\theta \right) - \theta_{n-2} \frac{G_{\theta 2}}{h^2} \\
& - \frac{G_{z\alpha 1}}{h^{\alpha+1}} \sum_{j=1}^{n} w_j^{(\alpha+1)} z_{n-j} - \frac{G_{z\beta 1}}{h^{\beta+1}} \sum_{j=1}^{n} w_j^{(\beta+1)} z_{n-j} \\
& - \frac{G_{\theta\alpha 2}}{h^{\alpha+2}} \sum_{j=1}^{n} w_j^{(\alpha+2)} \theta_{n-j} - \frac{G_{\theta\alpha 1}}{h^{\alpha+1}} \sum_{j=1}^{n} w_j^{(\alpha+1)} \theta_{n-j} - \frac{G_{\theta\alpha}}{h^{\alpha}} \sum_{j=1}^{n} w_j^{(\alpha)} \theta_{n-j} \\
& - \frac{G_{\theta\beta 2}}{h^{\beta+2}} \sum_{j=1}^{n} w_j^{(\beta+2)} \theta_{n-j} - \frac{G_{\theta\beta 1}}{h^{\beta+1}} \sum_{j=1}^{n} w_j^{(\beta+1)} \theta_{n-j} - \frac{G_{\theta\beta}}{h^{\beta}} \sum_{j=1}^{n} w_j^{(\beta)} \theta_{n-j} \\
& + M_{bn} \left(1 + 2a\frac{r^\alpha}{h^\alpha} + 2b\frac{r^\beta}{h^\beta} \right) + 2a\frac{r^\alpha}{h^\alpha} \sum_{j=1}^{n} w_j^{(\alpha)} M_{bn-j} + 2b\frac{r^\beta}{h^\beta} \sum_{j=1}^{n} w_j^{(\beta)} M_{bn-j}
\end{aligned}
\tag{47}
$$

The coefficents are given in Appendix A2.

Finally, the system that has to be solved can be written in the following form given by Equation (48):

$$
\boldsymbol{A} \begin{pmatrix} z_n \\ \theta_n \end{pmatrix} = \boldsymbol{b} \tag{48}
$$

For Swinney's model, the equations are the same but all coefficients that contain b and β disappear.

Based on the previous mathematical developments for the Jones' model and fractional derivatives models, it can be observed that the final form of the system is the same. Indeed, by starting from the same equations, it is obvious that all models provide a similar formulation. However, the fractional derivatives mathematical expression does not require augmented states. Then, it is possible to create a numerical data bank for each model and solve different types of equations systems without further work from an engineer. On the one hand, fractional derivatives mathematical development is more adaptable if the model is modified but on the other hand, the sum calculation is time-consuming while augmented states have a finite memory.

On Figures 21, 22, 23, 24, 25, 26, 27, 28 and 29, the PSD for each model and for three different steps are plotted. The full lines represent the Theodorsen's function in frequency domain while the dashed lines are for the Monte Carlo approach for each model approximation.

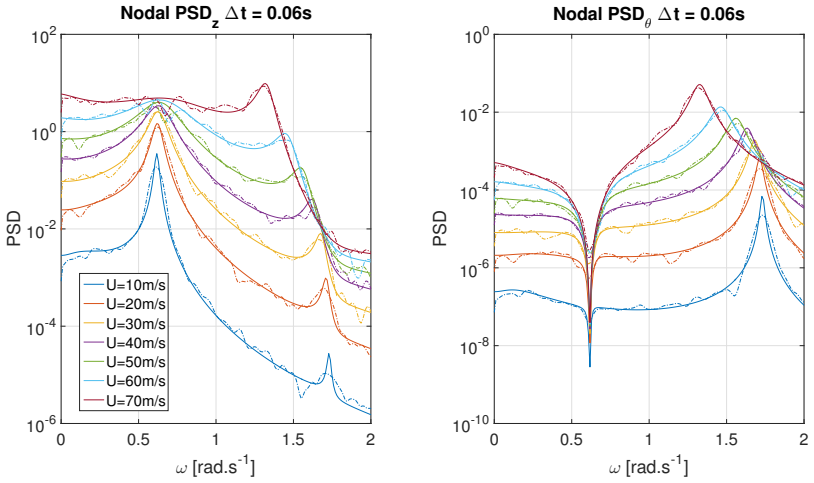

Figure 21: PSD given by Jones' model $\Delta t = 0.06s$

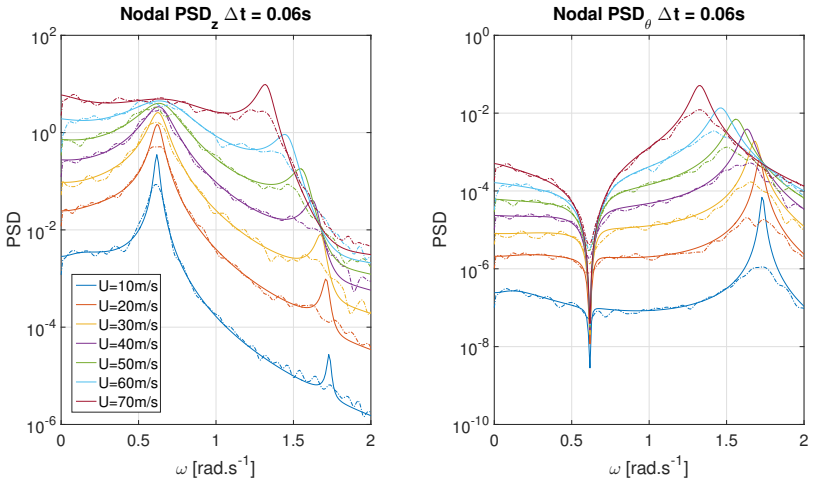

Figure 22: PSD given by Swinney's model $\Delta t = 0.06s$

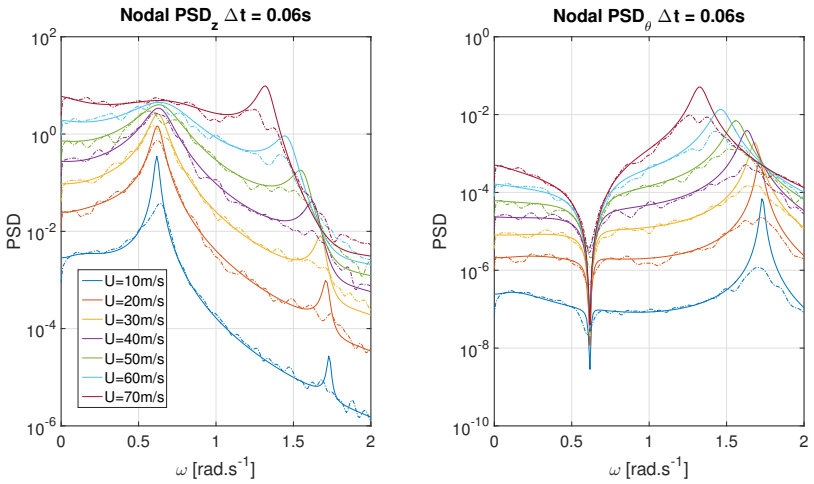

Figure 23: PSD given by augmented Swinney's model $\Delta t = 0.06s$

On Figures 21, 22 and 23, the only model approximation that practically fits the reference function is the Jones' model. For the fractional derivatives models, the curves are heterogeneous, especially around the peaks. The time step is too big for these models.

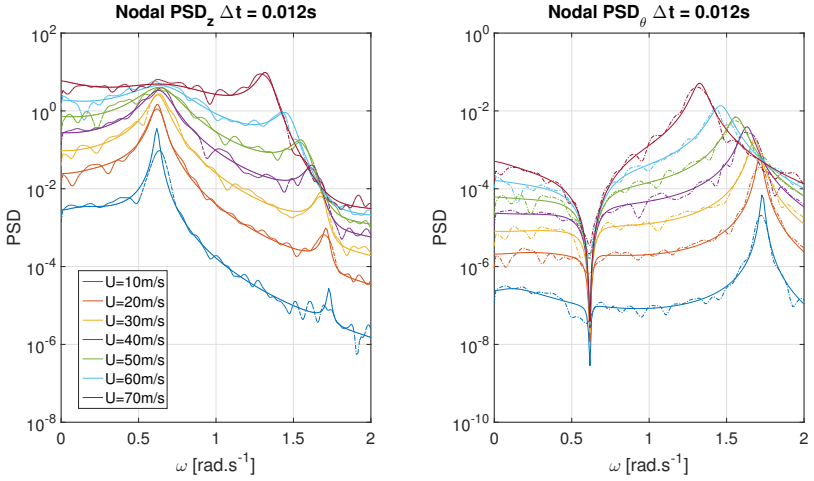

Figure 24: PSD given by Jones' model $\Delta t = 0.012s$

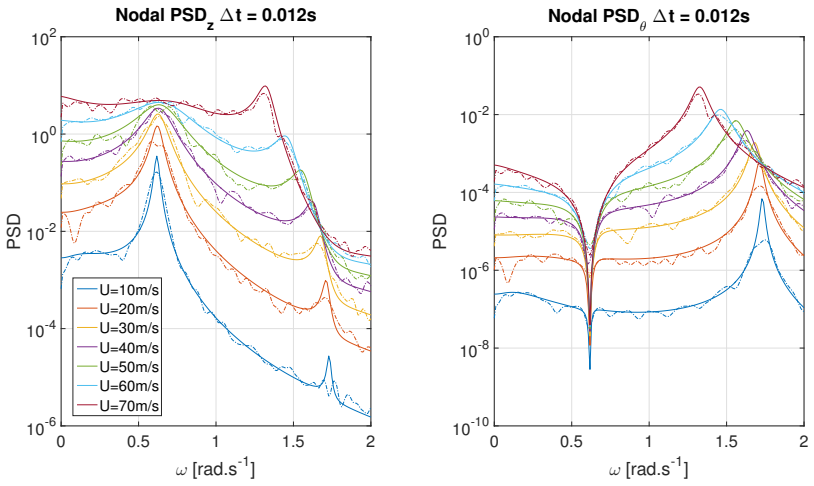

Figure 25: PSD given by Swinney's model $\Delta t = 0.012s$

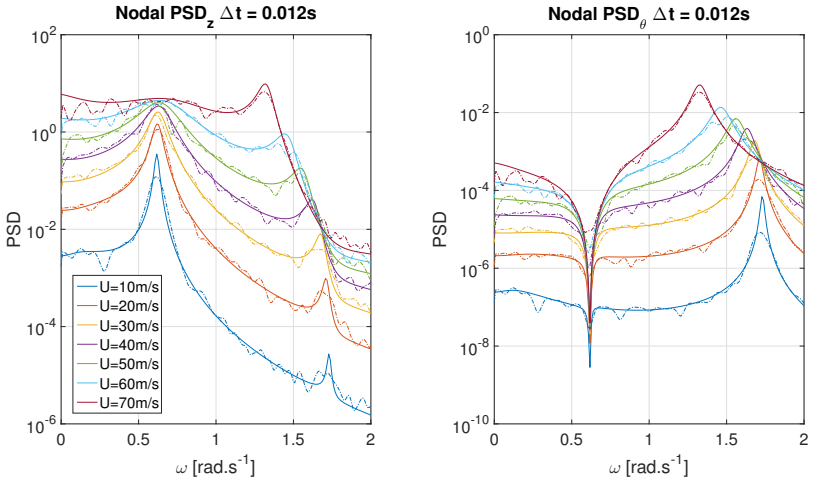

Figure 26: PSD given by augmented Swinney's model $\Delta t = 0.012s$

On Figures 24, 25 and 26, by reducing the time step, the fitting of the fractional derivatives models is improved. The peaks are now visible for all models but Jones' model is still the most accurate one for this time step.

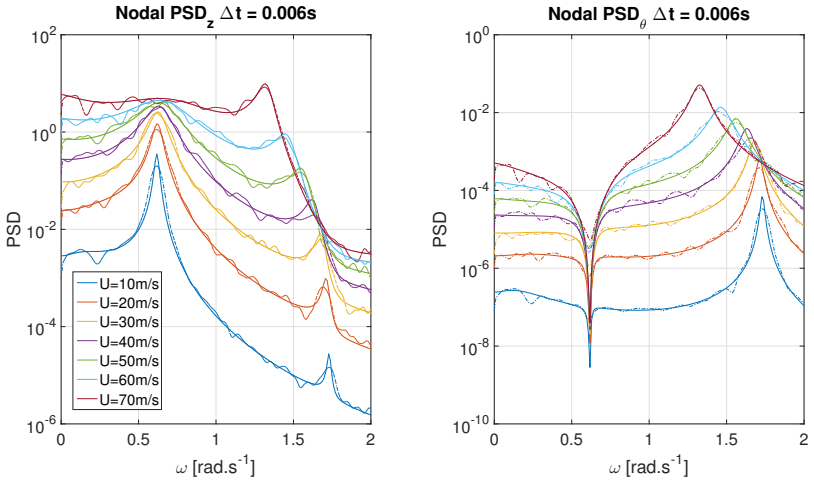

Figure 27: PSD given by Jones' model $\Delta t = 0.006s$

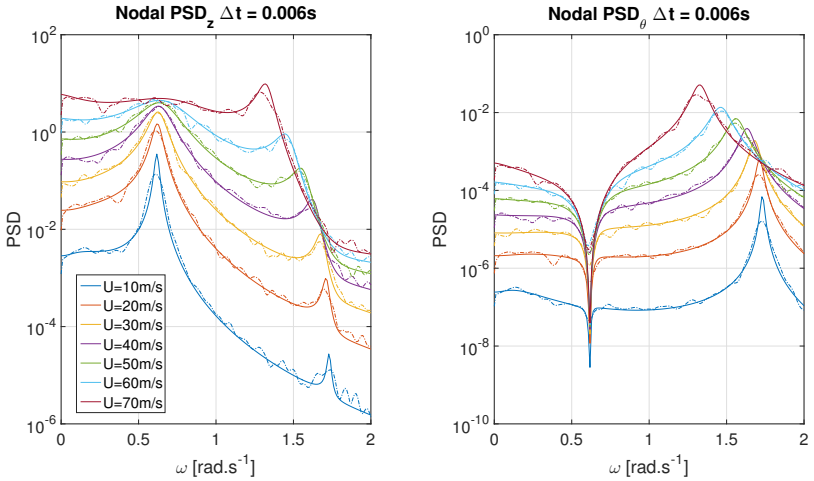

Figure 28: PSD given by Swinney's model $\Delta t = 0.006s$

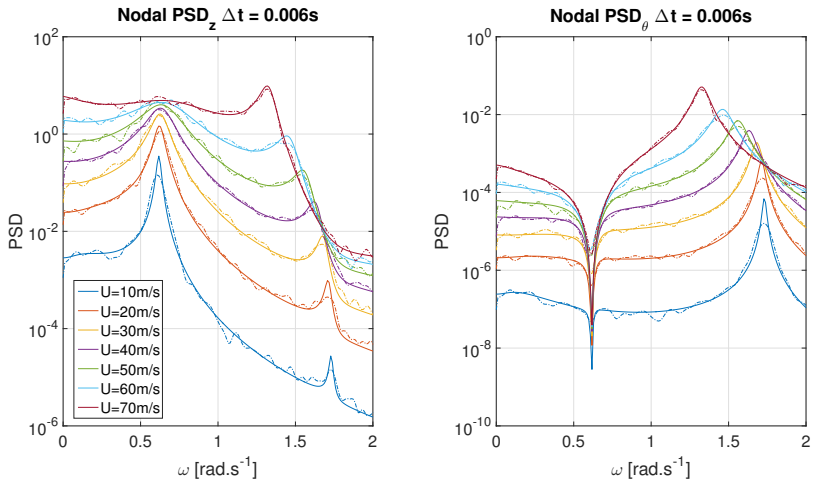

Figure 29: PSD given by augmented Swinney's model $\Delta t = 0.006s$

The smaller the time step, the better the matching. On Figures 27, 28 and 29, all models approximations give good results of the reference PSD but the peaks fitting are smoother for Jones' and augmented Swinney's models. For a time step $\Delta t = 0.006s$, all models have converged to an accurate solution.

On Figures 30, 31, 32, 33, 34, 35, 36, 37 and 38, the standard deviation σ is plotted for all models and for three different time steps. It is important to notice that $[\sigma_z] \neq [\sigma_\theta]$. This is why σ_θ has been multiplied by $\frac{B}{2}$ in order to be able to compare both standard deviations.

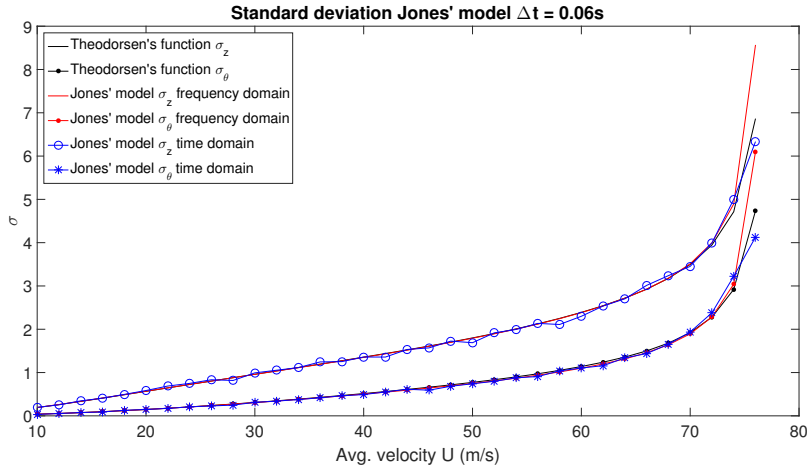

Figure 30: Standard deviation given by Jones' model $\Delta t = 0.06s$

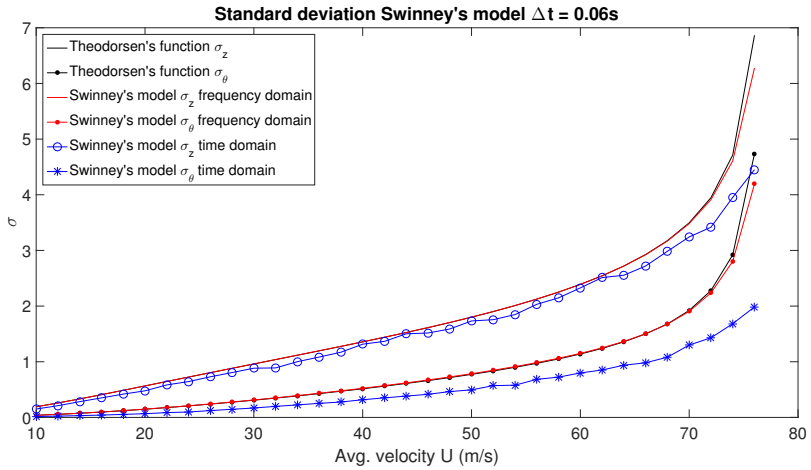

Figure 31: Standard deviation given by Swinney's model $\Delta t = 0.06s$

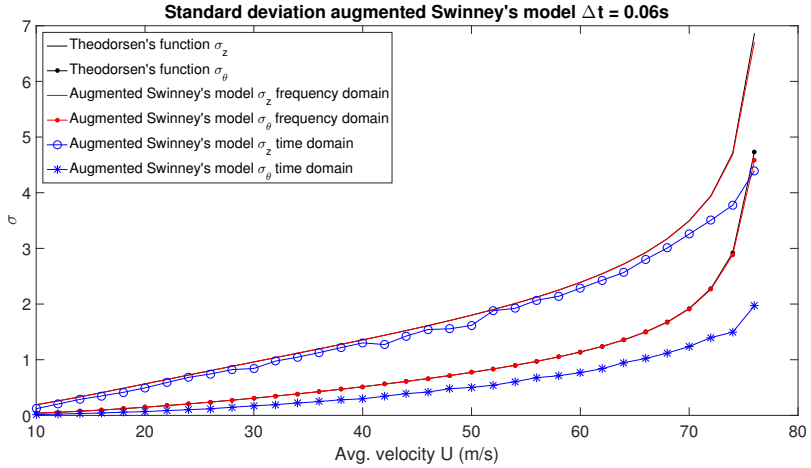

Figure 32: Standard deviation given by augmented Swinney's model $\Delta t = 0.06s$

On Figures 30, 31 and 32, the observations made for the PSD are the same. The Jones' model fits to a great extent its standard deviation in the frequency domain while both fractional derivatives models are inaccurate.

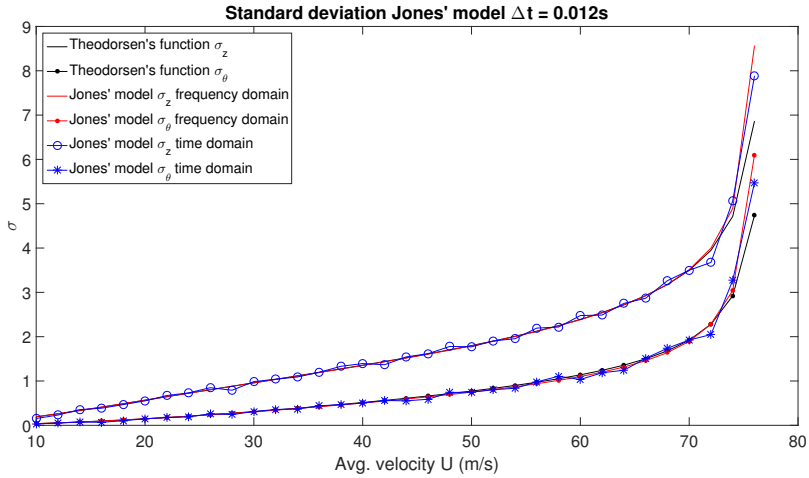

Figure 33: Standard deviation given by Jones' model $\Delta t = 0.012s$

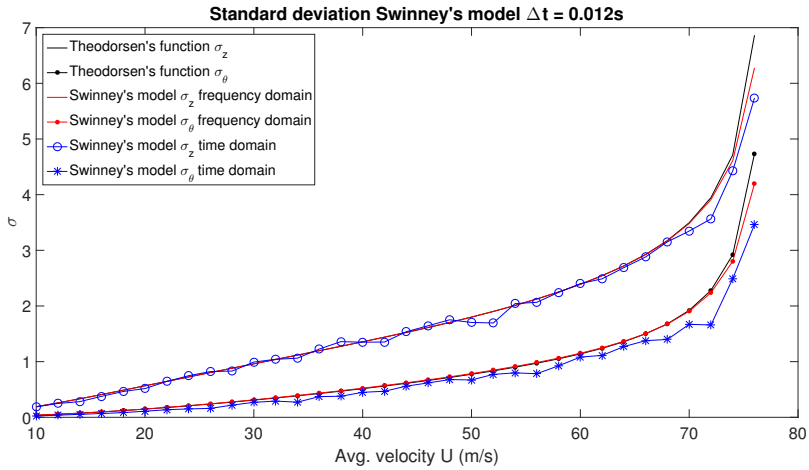

Figure 34: Standard deviation given by Swinney's model $\Delta t = 0.012s$

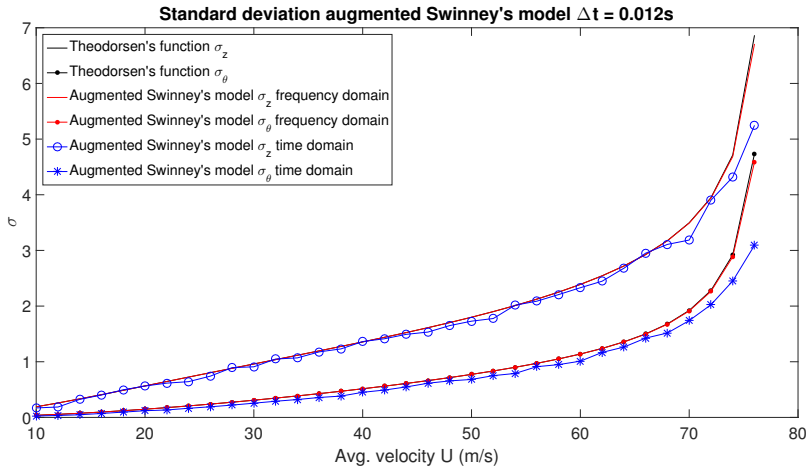

Figure 35: Standard deviation given by augmented Swinney's model $\Delta t = 0.012s$

On Figures 33, 34 and 35, the fractional derivatives models start fitting their standard deviations in the frequency domain except for high wind speed values.

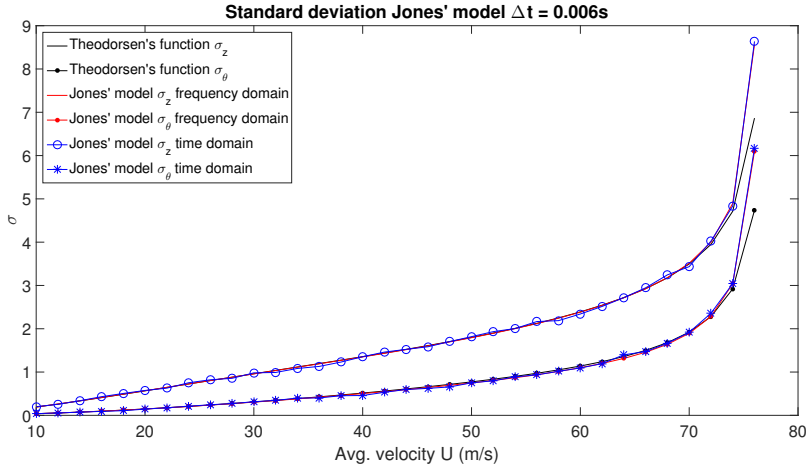

Figure 36: Standard deviation given by Jones' model $\Delta t = 0.006s$

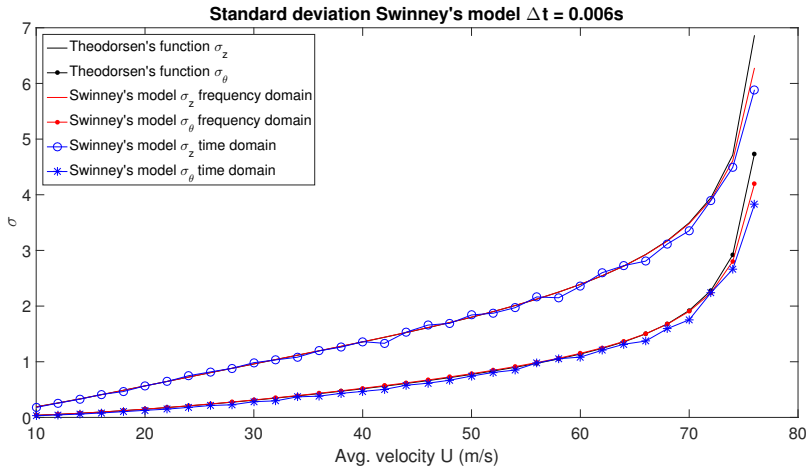

Figure 37: Standard deviation given by Swinney's model $\Delta t = 0.006s$

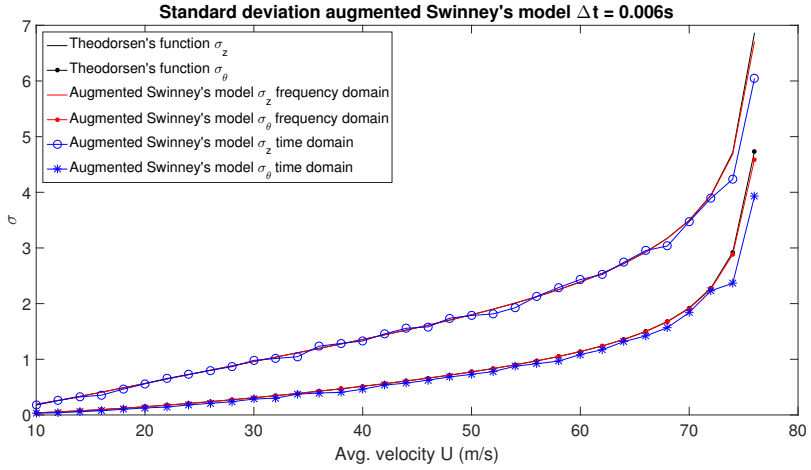

Figure 38: Standard deviation given by augmented Swinney's model $\Delta t = 0.006s$

On Figures 36, 37 and 38, all models are accurate. The Jones' model fits perfectly with its standard deviation in the frequency domain. For both fractional derivatives models, the numerical solution in the time domain is good but it can be observed that the standard deviation σ_θ is always underestimated.

On Figures 39, 40 and 41, the error of standard deviations is plotted compared to the standard deviation given by Theodorsen's function for three different time steps. Again, it has been decided to compare the obtained wind speed values for a given standard deviation.

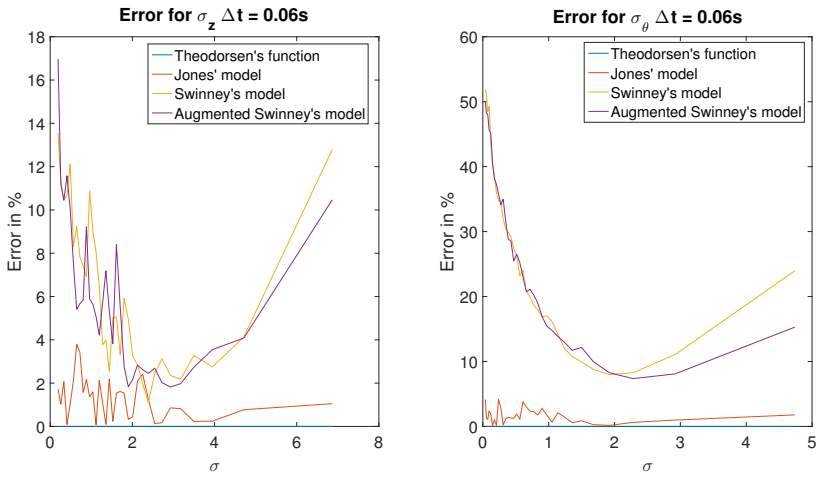

Figure 39: Standard deviation error $\Delta t = 0.06s$

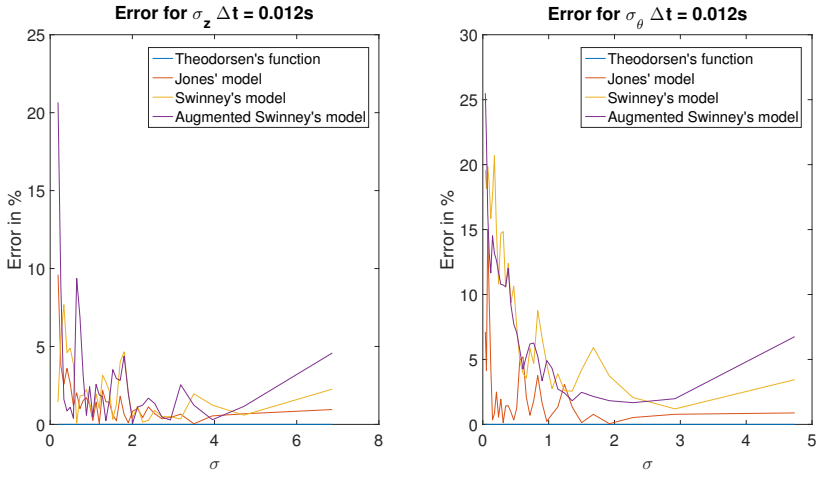

Figure 40: Standard deviation error $\Delta t = 0.012s$

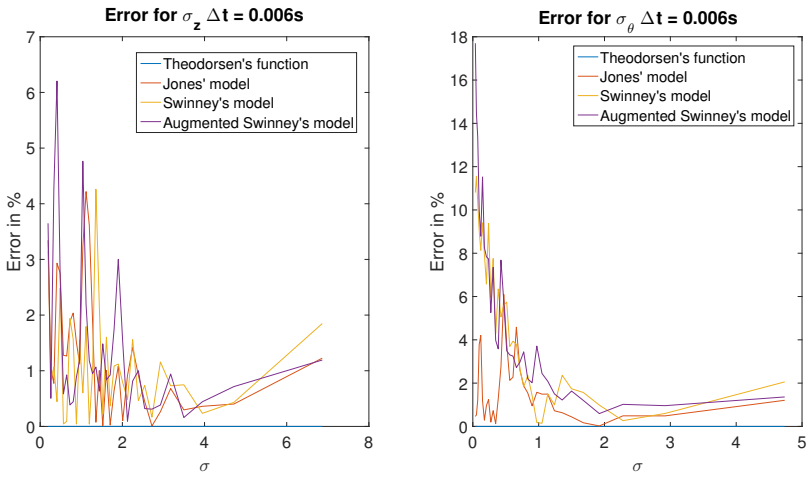

Figure 41: Standard deviation error $\Delta t = 0.006s$

Based on Figures 39, 40 and 41, as expected, the smaller the time step, the smaller the error. For all different time steps, Jones' model error is more or less the same around 5%. For the fractional derivatives models, the error is pretty big for the two first time steps. For $\Delta t = 0.006s$, the fractional derivatives errors are quite close to Jones' error even if the standard deviation error σ_θ of fractional derivatives models is high for small values of σ. It comes from the fact that the standard deviation σ_θ is always underestimated, as mentioned above for Figures 37 and 38.

Numerical calculation time

The accuracy of the different models has been much discussed in the previous sections. In this one, the numerical calculation time of one standard deviation for each model is analysed thanks to the Figure 42.

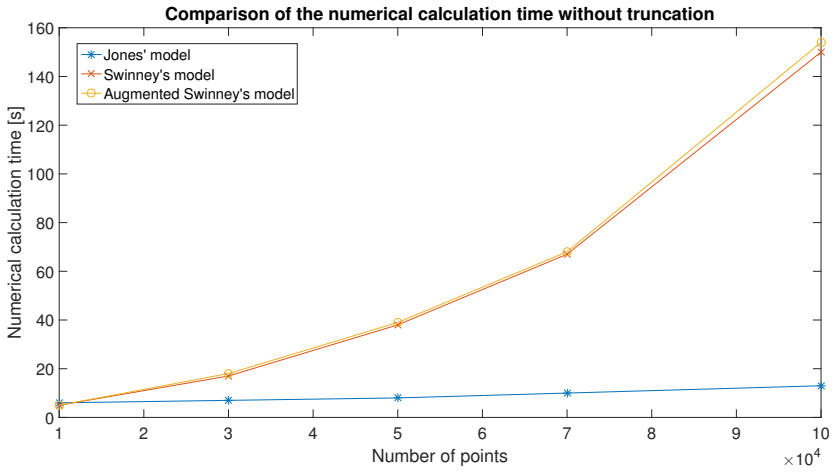

Figure 42: Comparison of the numerical calculation time without truncation

On Figure 42, the x-axis represents the number of points. The more points there are, the smaller the time step is. Increasing the number of points raises slightly the numerical calculation time for the Jones' model. Unfortunately, the numerical calculation time increases sharply for both fractional derivatives models. Indeed, based on the formulation of Grünwald-Letnikov (see Equation (9)), the sum has to be calculated again for each step and the number of elements inside the sum increases for each step too. Due to these two factors, the numerical calculation time for fractional derivatives models is very high. For $N = 100000$, this time is ten times greater than the one of Jones' model for the same accuracy as shown in the previous section.

Optimisation and truncation

As mentioned in the previous section, the numerical calculation time is very high for fractional derivatives models. A good optimisation is to truncate the sum. The idea behind this concept is the 'Short-Memory' Principle [2]. It means that the current time step depends only on the 'recent past'. Thanks to this assumption, it is possible to limitate the maximum numbers of elements inside the sum to spare some calculation time without decreasing too much the accuracy of both models.

On Figures 43, 44 and 45, the numerical calculation time is plotted for different time steps Δt and for different maximum values of elements inside the sum of the fractional derivatives models.

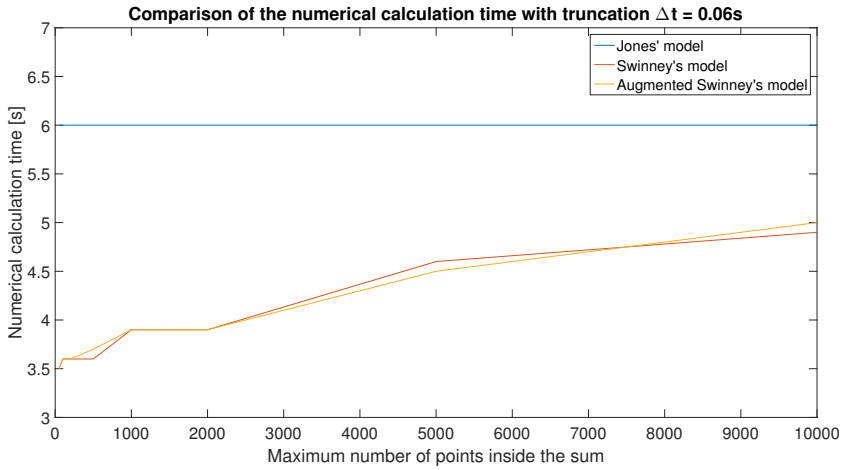

Figure 43: Comparison of the numerical calculation time with truncation $\Delta t = 0.06s$

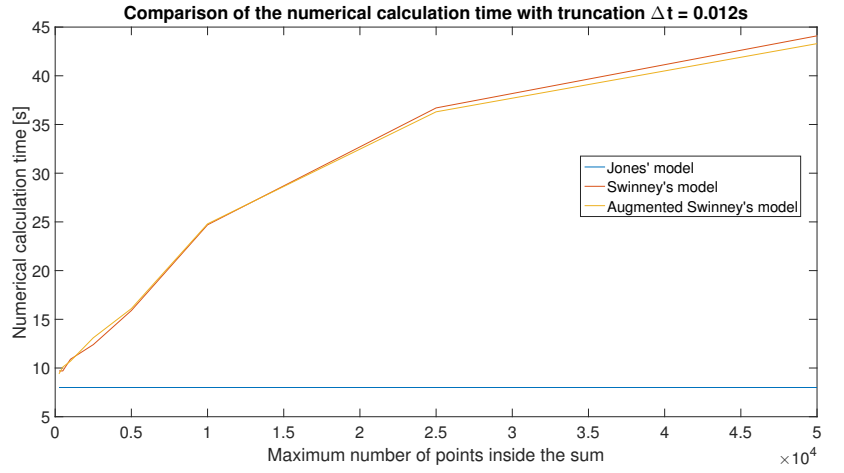

Figure 44: Comparison of the numerical calculation time with truncation $\Delta t = 0.012s$

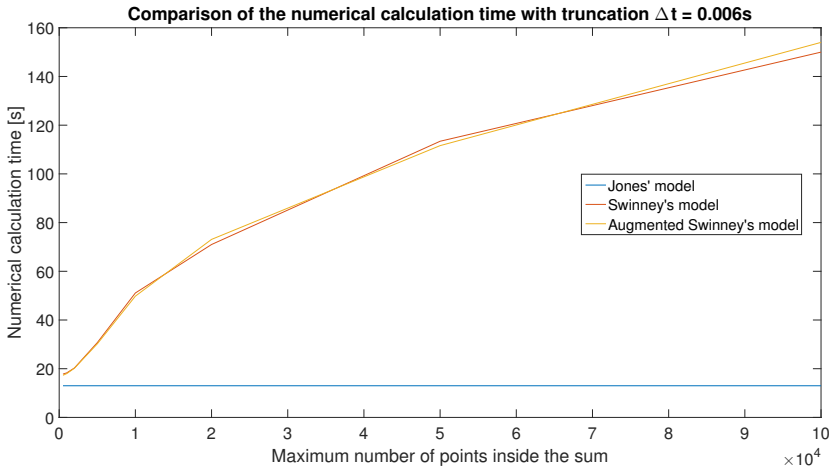

Figure 45: Comparison of the numerical calculation time with truncation $\Delta t = 0.006s$

On Figure 43, the numerical calculation time for both fractional derivatives models is always smaller than the numerical calculation time of Jones' model with and without truncation. However, it has been mentioned that for this time step, the accuracy of the fractional derivatives models is lower compared to Jones' model.

On Figures 44 and 45, the opposite is observed. Nonetheless, by limiting the maximum numbers of elements inside the sum of fractional derivatives models, the numerical calculation time tends to the numerical calculation time of Jones' model.

To choose the correct maximum number, it is also interesting to check how the accuracy varies due to the truncation. On Figures 46, 47 and 48, the standard deviation error due to truncation is shown for different time steps and the formula of the error is given by Equation (49).

$$error = \sqrt{\sum \left(\sigma_{\text{Theodorsen}} - \sigma_{\text{Model}}\right)^2} \tag{49}$$

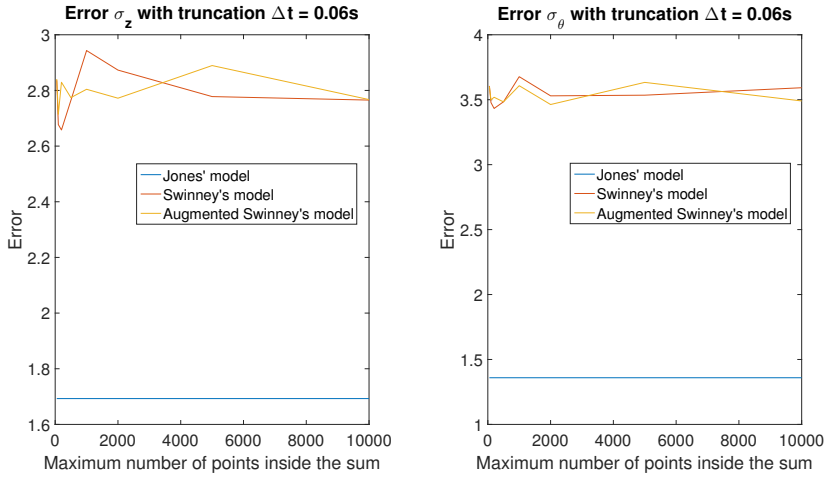

Figure 46: Standard deviation σ error due to truncation $\Delta t = 0.06s$

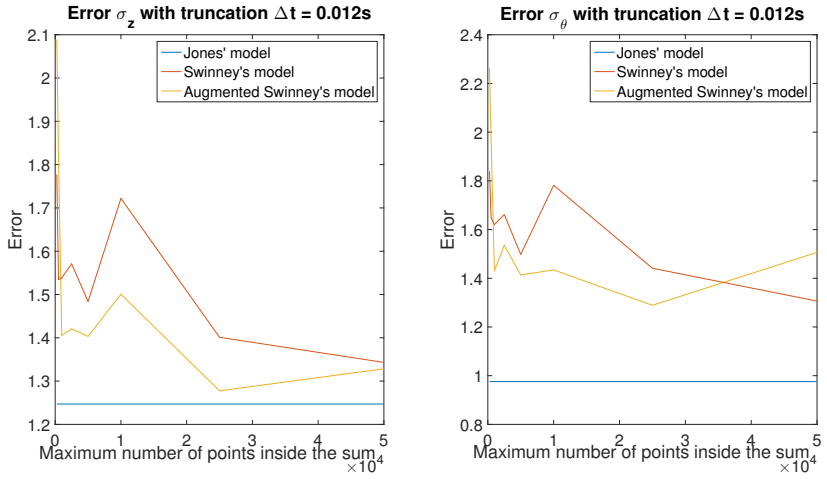

Figure 47: Standard deviation σ error due to truncation $\Delta t = 0.012s$

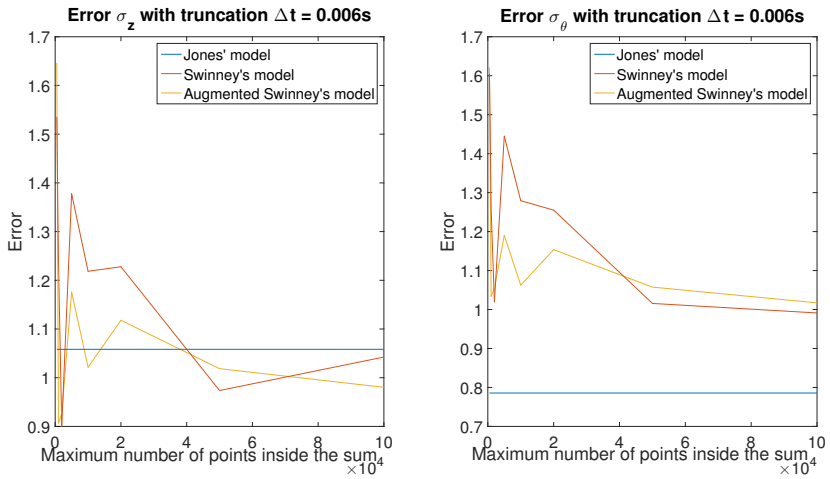

Figure 48: Standard deviation σ error due to truncation $\Delta t = 0.006s$

On Figure 46, the error for both fractional derivatives models is greater than the error of Jones' model for all maximum number of points inside the sum.

On Figure 47, the error for fractional derivatives models is smaller compared to the one on Figure 46. As expected, for small maximum numbers of elements inside the sum, the accuracy of the fractional derivatives models decreases. Nevertheless, it exists a fluctuation of the error values due to Monte Carlo simulations.

On Figure 48, the error of σ_z for both fractional derivatives models is close to the error of Jones' model. However, for σ_θ, it is the opposite. Again, for small maximum numbers inside the sum, the accuracy is reduced.

To summarize this section, a truncation of a maximum number of elements of $N/50$ is a good compromise between accuracy and numerical time calculation where N is the maximum time simulation over the time step. As an example, if the simulation lasts $600s$ and $\Delta t = 0.06s$ thus $N = \frac{600}{0.06} = 10000$ and then the maximum number of elements inside the sum is equal to 200.

5 Application of a case study : The Golden Gate Bridge

In Chapter 4, the flutter speed has been calculated for the flat plate theory by using the data of the Storebaelt Bridge. In this chapter, the fractional derivatives models are used to calculate the flutter speed for the Golden Gate Bridge. Firstly, the Scanlan's flutter derivatives are approximated by all models. For the Jones' model, the traditional definition of the Scanlan's flutter derivatives is used while the Starossek's formulation is applied for fractional derivatives models. Then, the flutter speed is determined in the frequency domain for single degree-of-freedom θ. A comparison between each model is carried out. Finally, in the time domain, the flutter speed is calculated.

5.1 Fitting of the Scanlan's flutter derivatives

The Theodorsen's function is only applicable to the flat plate theory. In this chapter, Scanlan's flutter derivatives have to be used. They are obtained experimentally [18]. For each models' fitting, the function minimizes the error given by Equation (30). For the Jones' model, the standard definition of Scanlan's flutter derivatives is used (see Equation (26)). Only A_2^* and A_3^* have to be approximated because single degree-of-freedom θ is taken into account.

Figures 49 and 50 show the Jones' fitting.

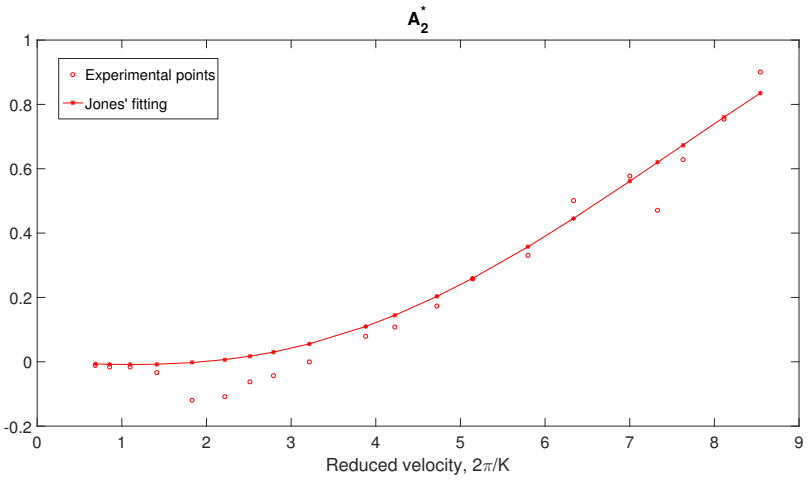

Figure 49: A_2^* Jones' model

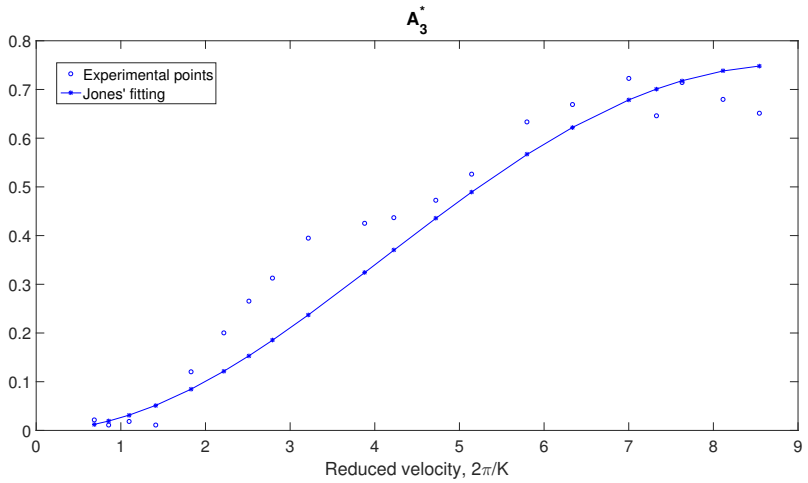

Figure 50: A_3^* Jones' model

On Figures 49 and 50, Jones' model with four parameters was used. By definition, a_0 is always equal to 1. The values of these parameters are given in Table 4.

Jones' coefficients	Values
a_1	1.1512
b_1	0.3711
a_2	-1.2873
b_2	0.0511

Table 4: Jones' coefficients for the fitting of Scanlan's derivatives A_2^* and A_3^*

For the fractional derivatives models, the equations were extended in a more general way. The new formulas for both models are given by Equations (50) and (51).

$$S(k) = \frac{1 + a(ik)^\alpha}{1 + b(ik)^\alpha} \tag{50}$$

$$S_{aug}(k) = \frac{1 + a(ik)^\alpha + c(ik)^\beta}{1 + b(ik)^\alpha + d(ik)^\beta} \tag{51}$$

On Figures 51 and 52, the fitting of Swinney's model for A_2^* and A_3^* is plotted.

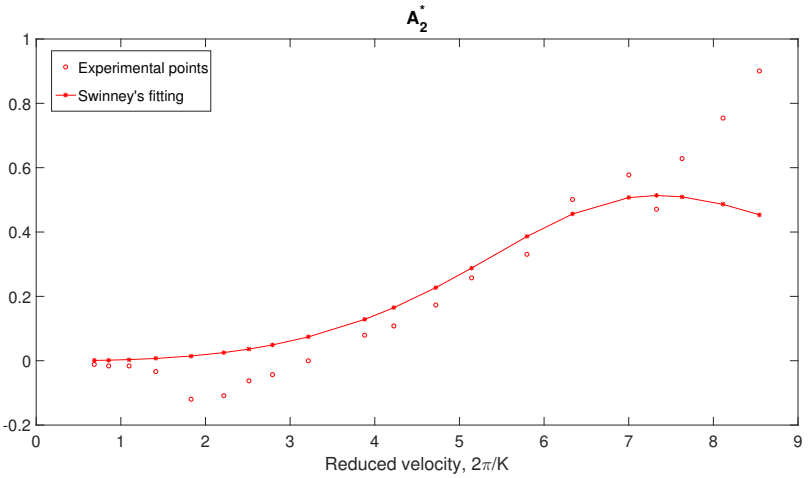

Figure 51: A_2^* Swinney's model

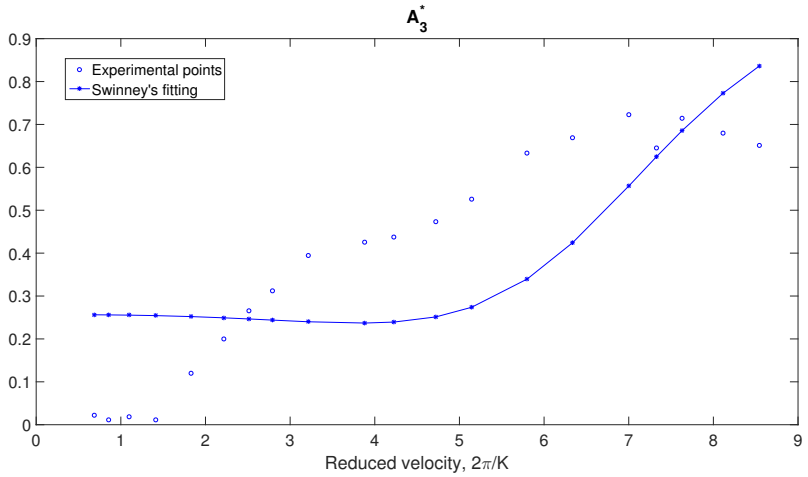

Figure 52: A_3^* Swinney's model

The coefficients of the Swinney's model are given in Table 5.

Swinney's coefficients	Values
a	2.7616
b	10.7557
α	2.7970

Table 5: Swinney's coefficients for the fitting of Scanlan's derivatives A_2^* and A_3^*

Based on Figures 51 and 52, it can be observed that the Swinney's model does not fit with the experimental points. Indeed, the number of parameters is not enough. By increasing this number, the fitting is better.

On Figures 53 and 54, the fitting of the augmented Swinney's model for Scanlan's flutter derivatives is plotted.

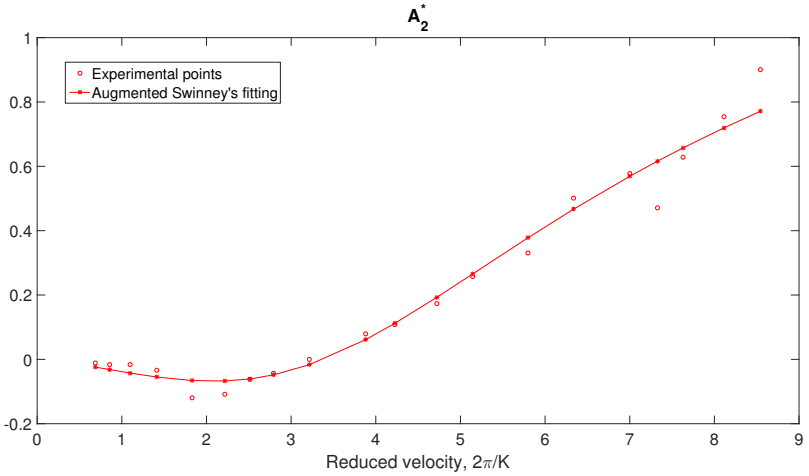

Figure 53: A_2^* Augmented Swinney's model

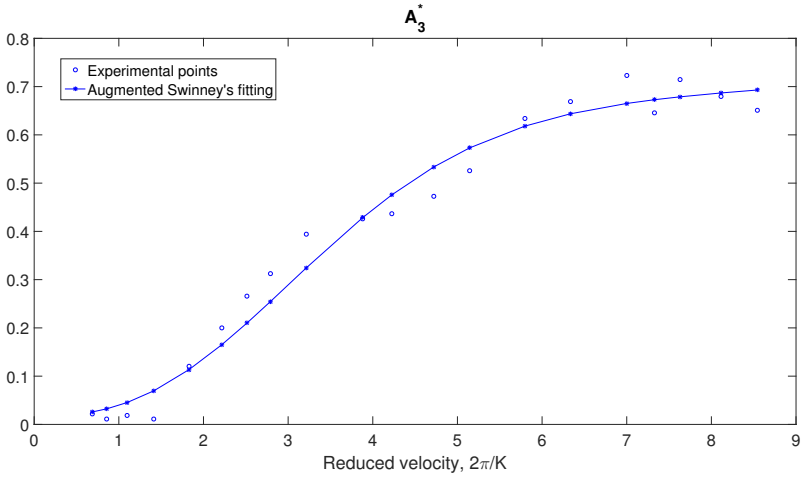

Figure 54: A_3^* Augmented Swinney's model

The augmented Swinney's model values are given in Table 6.

Augmented Swinney's coefficients	Values
a	-0.9955
b	-1.0128
c	-0.008
d	-0.0385
α	0.0063
β	1.6201

Table 6: Augmented Swinney's coefficients for the fitting of Scanlan's derivatives A_2^* and A_3^*

As expected, by increasing the number of parameters of the model, the fitting of the experimental points is better. The best fitting is obtained by augmented Swinney's model, followed by Jones' model and Swinney's model.

5.2 Frequency domain

In the previous section, the Scanlan's flutter derivatives A_2^* and A_3^* were determined for all models. In this section, the PSD and the standard deviations given by all models are analysed.

The Golden Gate Bridge characteristics are given in Table 7 (see [18]).

	Value	Unit
J	$4.4 \cdot 10^6$	$kg \cdot m^2/m$
B	27.43	m
ξ	0.005	$-$
f_θ	0.1916	Hz
ρ	1.22	kg/m^3
L_w	20	m
I_w	0.05	$-$

Table 7: Golden Gate Bridge values

As mentioned in the previous section, the traditional formulation of Scanlan's flutter derivatives is used for the Jones' model. Single degree-of-freedom is considered in this analysis. The self-excited force M_{se} is simplified and its mathematical formula is given by Equation (52).

$$M_{se}(\omega) = qB^2 \left[KA_2^*(K)\frac{B(i\omega)\theta(\omega)}{U} + K^2 A_3^*(K)\theta(\omega) \right] \tag{52}$$

For both fractional derivatives models, the Starossek's formulation is applied. The self-excited force M_{se} mathematical formula for these two models is given by Equation (53).

$$M = \omega^2 \pi \rho b^4 c_{\theta\theta} \theta \tag{53}$$

On Figure 55, the standard deviation given by the different models is shown.

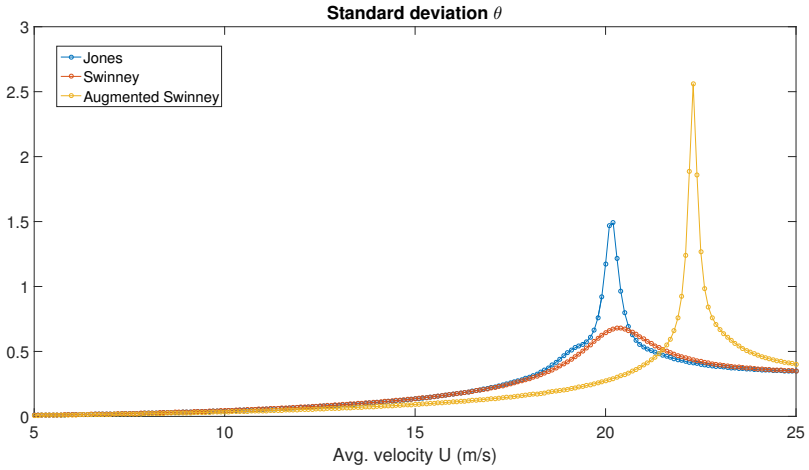

Figure 55: Standard deviation given by the different models for the Golden Gate Bridge in frequency domain

The values of the flutter speed for each model are given in Table 8.

Models	Flutter speed [m/s]
Jones	20.2
Swinney	20.3
Augmented Swinney	22.3

Table 8: Flutter speed given by each model for the Golden Gate Bridge

Based on Figure 55 and Table 8, the flutter speed is similar for each model. Indeed, the maximum difference is equal to 2 m/s. Moreover, even if the flutter speed for all models is low, it stays inside the values range for the given data in Table 7 (see[18]).

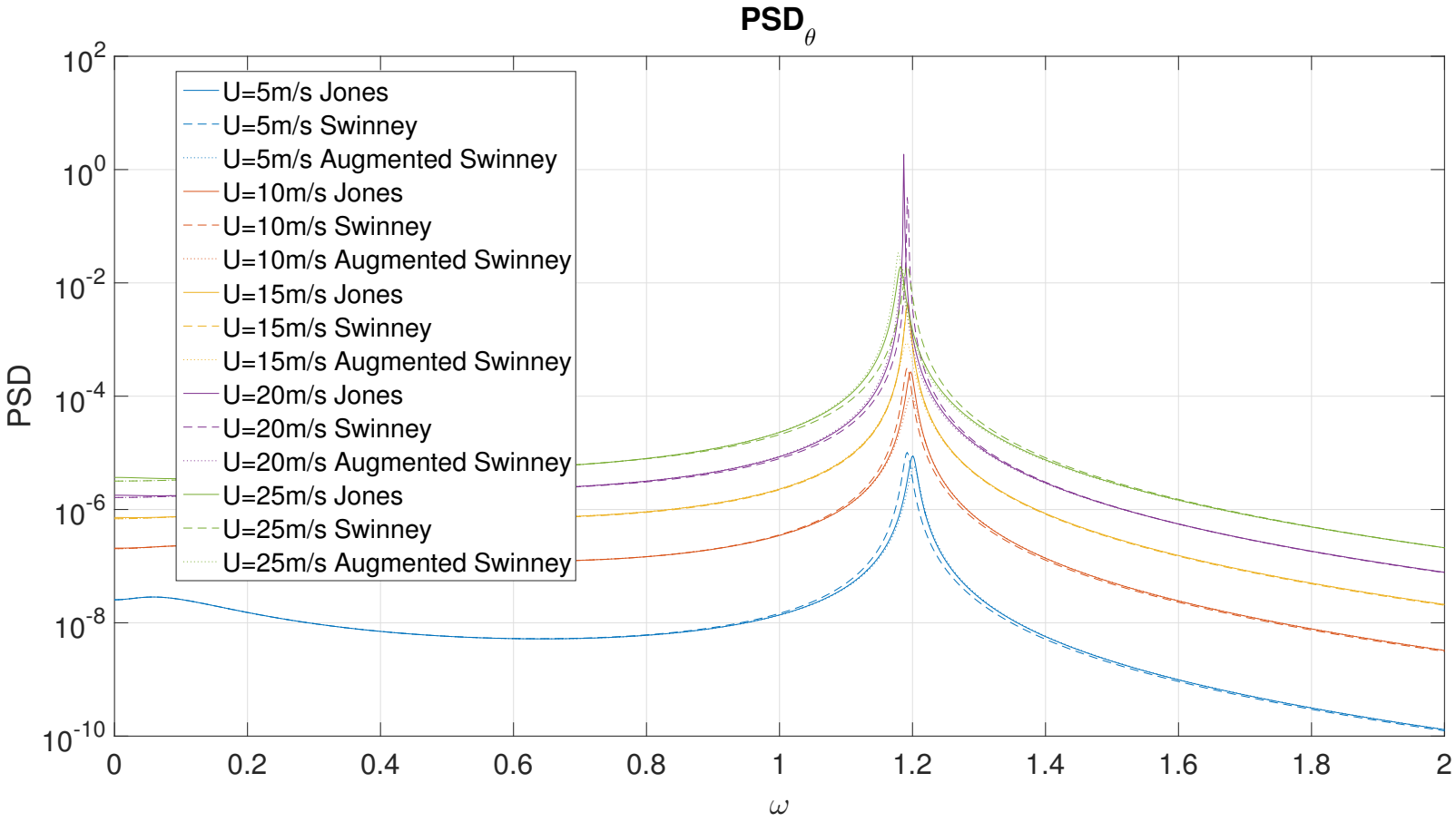

Figure 56: PSD given by the different models for the Golden Gate Bridge in frequency domain

On Figure 56, it is possible to see that the PSD given by the models are close to each other, except for the peaks. Indeed, they are not equal in terms of magnitude and location. This variation explains the difference of the flutter speed given by each model. However, the structural response and the behaviour of the structure are properly calculated.

5.3 Time domain

The same method as the one described in section 4.3 is used. Unfortunately, both fractional derivatives models do not converge to a finite solution. A deepened stability analysis of the Grünwald-Letnikov definition is needed in order to study the models' convergence for many parameters values.

6 Conclusions

The objective of this Master thesis is to investigate the modeling of bridge deck flutter by means of fractional derivatives. Through this work, the flat plate theory and a case study of the Golden Gate Bridge were being analysed.

The main results of the flat plate theory are summarized below :

- The augmented Swinney's model's approximation shows the best fitting of the Theodorsen's function. The advantage of this model compared to the Jones' model is that it uses the same number of parameters.
- In the frequency domain, the augmented Swinney's response properly fits with the results returned by the Theodorsen's function. However, the difference of the flutter speeds given by all models is low. Moreover, the error on the flutter speed for a given standard deviation is maximum for the Jones' model and is equal to 1.5% while this error is barely equal to 0.4% for the augmented Swinney's model.
- The mathematical expressions for both fractional derivatives models are easily adaptable and a numerical data bank can be used in order to solve different problems. However, the required memory for these models is greater than the one for the Jones' model; these models are more time-consuming.
- In the time domain, both fractional derivatives models need a smaller time step to achieve the same accuracy as the one of Jones' model. Moreover, the smaller the time step is, the greater the numerical time is required. Indeed, due to a smaller time step, the number of elements inside the fractional derivatives sum is greater which greatly increases the numerical calculation time. A truncation of the sum can be carried out. By limiting the number of elements to $N/50$, where N is the ratio between the maximum simulation time and the time step, the accuracy remains the same while the numerical calculation time is greatly reduced.

For the Golden Gate Bridge, the following results can be listed :

- The parameters of both fractional derivatives models have been increased in order to improve the Scanlan's flutter derivatives fitting. The augmented Swinney's model provides the best matching of the experimental points, followed by the Jones' and Swinney's models.
- In the frequency domain, the flutter speeds given by all models are slightly different due the variation of the PSD peaks magnitude.

Finally, fractional derivatives models offer a great extension to integer derivatives models, like the Jones' model, in order to investigate on the modeling of bridge deck flutter thanks to the accuracy improvement of flutter speed results.

Further research

- Detailed research could be undertaken on the fitting of Scanlan's flutter derivatives in order to compare fractional derivatives models and integer derivatives models. The number of used parameters and the accuracy of each model should be investigated.
- Further research could also be made on the numerical fractional derivatives scheme to determine the numerical stability based on parameters values.

Personal contributions

- The improvement of the Theodorsen's function approximation by using the augmented Swinney's model.
- The comparison between fractional derivatives models and Jones' model in order to compute the flutter speed thanks to the stochastic analysis.
- The numerical implementation of fractional derivatives models and the study of its truncation.
- The fitting of Scanlan's flutter derivatives by combining fractional derivatives models and Starossek's formulation.

References

[1] Y. Tamura A. Kareem, editor. *Advanced Structural Wind Engineering*. Springer, 2013.

[2] I. Podlubny. *Fractional Differential Equations*, volume 198. Academic Press, 1998.

[3] G. Piccardo G. Solari. Probabilistic 3-d turbulence modeling for gust buffeting of structures. *Probabilistic Engineering Mechanics*, 16:73–86, 2001.

[4] Massimiliano Zingales Giuseppe Failla. Advanced materials modelling via fractional calculus: challenges and perspectives. *Philosophical Transactions of the Royal Society*, 378, 2020.

[5] Marc Weilbeer. *Efficient Numerical Methods for Fractional Differential Equationsand their Analytical Background*. PhD thesis, Technischen Universität Braunschweig, 2005.

[6] Igor Podlubny. Matrix approach to discrete fractional calculus. *Fractional Calculus and Applied Analysis*, 3(4), 2000.

[7] Devendra Chouhan Raghvendra S. Chandel, Amardeep Singh. Numerical solution of fractional relaxation-oscillation equation using cubib b-spline wavelet collocation method. *Italian Journal of Pure and Applied Mathematics*, 36:399–414, 2016.

[8] Guido Morgenthal Tajammal Abbas, Igor Kavrakov. Methods for flutter stability analysis of long-span bridges : a review. *Bridge Engineering*, 170:271–310, 2017.

[9] Charalambos C. Baniotopoulos Ted Stathopoulos, editor. *Wind effects on buildings and design of wind-sensitive structures*. Springer, 2009.

[10] V. Denoël. Analyse de structures 2 (syllabus de master 1), volume 1,. *Faculté des Sciences appliquées, Université de Liège*, 2019.

[11] V. Denoël. Polynomial approximation of aerodynamic coefficients based on the statistical description of the wind incidence. *Probabilistic Engineering Mechanics*, 24:179–189, 2009.

[12] David V. Swinney. A fractional calculus model of aeroelasticity. Master's thesis, Air Force Institute of Technology, 1989.

[13] Robert T. Jones. The unsteady lift of a wing of finite aspect ratio. *NACA Technical Report 681*, 1940.

[14] N.P. Jones L. Caracoglia. Time domain vs. frequency domain characterization of aeroelastic forces for bridge deck sections. *Journal of Wind Engineering and Industrial Aerodynamics*, 91:371–402, 2003.

[15] Lydia Thiesemann Uwe Starossek, Hasan Aslan. Experimental and numerical identification of flutter derivatives for nine bridge deck sections. *Wind and Structures An International Journal*, 12(6), November 2009.

[16] Alex Pellegri Andrea Tornielli. A frequency domain method for buffeting analysis of long-span bridges. Master's thesis, 2018.

[17] V. Denoël. Eléments de processus stochastiques (syllabus de bac 3), volume 1,. *Faculté des Sciences appliquées, Université de Liège*, 2018.

[18] Vincent Denoël Thomas Canor, Luca Caracoglia. Application of random eigen value analysis to assess bridge flutter probability. *Wind Engineering and Industrial Aerodynamics*, 140:79–86, 2015.

Appendix

Appendix A1 Jones' model coefficients in time domain for the flat plate theory

$$\boldsymbol{M} = \begin{pmatrix} 1 & 0 & 0 & 0 & 0 & 0 & 0 & 0 & 0 & 0 \\ 0 & 1 & 0 & 0 & 0 & 0 & 0 & 0 & 0 & 0 \\ 0 & 0 & m + \frac{\pi\rho B^2}{4} & 0 & 0 & 0 & 0 & 0 & 0 & 0 \\ 0 & 0 & 0 & J + \frac{\pi\rho B^4}{128} & 0 & 0 & 0 & 0 & 0 & 0 \\ 0 & a_0 & 0 & 0 & 1 & 0 & 0 & 0 & 0 & 0 \\ 0 & a_1 & 0 & 0 & 0 & 1 & 0 & 0 & 0 & 0 \\ 0 & a_2 & 0 & 0 & 0 & 0 & 1 & 0 & 0 & 0 \\ 0 & 0 & -\frac{a_0}{U} & \frac{a_0 B}{4U} & 0 & 0 & 0 & 1 & 0 & 0 \\ 0 & 0 & -\frac{a_1}{U} & \frac{a_1 B}{4U} & 0 & 0 & 0 & 0 & 1 & 0 \\ 0 & 0 & -\frac{a_2}{U} & \frac{a_2 B}{4U} & 0 & 0 & 0 & 0 & 0 & 1 \end{pmatrix}$$

$$\boldsymbol{A} = \begin{pmatrix} 0 & 0 & 1 & 0 & 0 & 0 & 0 & 0 & 0 & 0 \\ 0 & 0 & 0 & 1 & 0 & 0 & 0 & 0 & 0 & 0 \\ -k_z & 0 & -c_z & \frac{qB}{4U} & q & q & q & q & q & q \\ 0 & -k_\theta & 0 & -c_\theta - \frac{qB^2}{16U} & \frac{qB}{4} & \frac{qB}{4} & \frac{qB}{4} & \frac{qB}{4} & \frac{qB}{4} & \frac{qB}{4} \\ 0 & 0 & 0 & 0 & -\frac{2Ub_0}{B} & 0 & 0 & 0 & 0 & 0 \\ 0 & 0 & 0 & 0 & 0 & -\frac{2Ub_1}{B} & 0 & 0 & 0 & 0 \\ 0 & 0 & 0 & 0 & 0 & 0 & -\frac{2Ub_2}{B} & 0 & 0 & 0 \\ 0 & 0 & 0 & 0 & 0 & 0 & 0 & -\frac{2Ub_0}{B} & 0 & 0 \\ 0 & 0 & 0 & 0 & 0 & 0 & 0 & 0 & -\frac{2Ub_1}{B} & 0 \\ 0 & 0 & 0 & 0 & 0 & 0 & 0 & 0 & 0 & -\frac{2Ub_2}{B} \end{pmatrix}$$

where $q = \pi\rho U^2 B$.

$$\boldsymbol{x}(t) = \begin{pmatrix} z(t) \\ \theta(t) \\ \dot{z}(t) \\ \dot{\theta}(t) \\ \mu_0 \\ \mu_1 \\ \mu_2 \\ \nu_0 \\ \nu_1 \\ \nu_2 \end{pmatrix}, \quad \boldsymbol{f}_b(t) = \begin{pmatrix} 0 \\ 0 \\ L_b(t) \\ M_b(t) \\ 0 \\ 0 \\ 0 \\ 0 \\ 0 \\ 0 \end{pmatrix}$$

Appendix A2 Augmented Swinney's model coefficients in time domain for the flat plate theory

$$F_{z2} = m + r^2 p$$
$$F_{z1} = 4\pi f_z \xi m + 2pr$$
$$F_z = 4\pi^2 f_z^2 m$$
$$F_{z\alpha 2} = 2ar^\alpha m + 2apr^{\alpha+2}$$
$$F_{z\alpha 1} = 8ar^\alpha \pi f_z \xi m + 2apr^{\alpha+1}$$
$$F_{z\alpha} = 8ar^\alpha \pi^2 f_z^2 m$$
$$F_{z\beta 2} = 2br^\beta m + 2bpr^{\beta+2}$$
$$F_{z\beta 1} = 8br^\beta \pi f_z \xi m + 2bpr^{\beta+1}$$
$$F_{z\beta} = 8br^\beta \pi^2 f_z^2 m$$
$$F_{\theta 1} = pBr$$
$$F_{\theta\alpha 1} = \tfrac{3}{2} apBr^{\alpha+1}$$
$$F_{\theta\beta 1} = \tfrac{3}{2} bpBr^{\beta+1}$$
$$F_\theta = pB$$
$$F_{\theta\alpha} = apBr^\alpha$$
$$F_{\theta\beta} = bpBr^\beta$$

$$G_{z1} = \tfrac{pB}{2} r$$
$$G_{z\alpha 1} = \tfrac{apB}{2} r^{\alpha+1}$$
$$G_{z\beta 1} = \tfrac{bpB}{2} r^{\beta+1}$$
$$G_{\theta 2} = J + \tfrac{pB^2}{32} r^2$$
$$G_{\theta 1} = 4\pi f_\theta \xi J$$
$$G_\theta = 4\pi^2 f_\theta^2 J - \tfrac{pB^2}{4}$$
$$G_{\theta\alpha 2} = 2ar^\alpha J + \tfrac{apB^2}{16} r^{\alpha+2}$$
$$G_{\theta\alpha 1} = 8ar^\alpha \pi f_\theta \xi J + \tfrac{apB^2}{8} r^{\alpha+1}$$
$$G_{\theta\alpha} = 8ar^\alpha \pi^2 f_\theta^2 J - \tfrac{apB^2}{4} r^\alpha$$
$$G_{\theta\beta 2} = 2br^\beta J + \tfrac{bpB^2}{16} r^{\beta+2}$$
$$G_{\theta\beta 1} = 8br^\beta \pi f_\theta \xi J + \tfrac{bpB^2}{8} r^{\beta+1}$$
$$G_{\theta\beta} = 8br^\beta \pi^2 f_\theta^2 J - \tfrac{bpB^2}{4} r^\beta$$